Materials Today Communications 48 (2025) 113185

Contents lists available at ScienceDirect

Materials Today Communications

journal homepage: www.elsevier.com/locate/mtcomm

Enhancement of fracture properties of amorphous polymers by nanoparticles: A machine-learning assisted coarse-grained model

Atiyeh Hente [a,*], Behrouz Arash [b,c], Maximilian Jux [d], Raimund Rolfes [a]

[a] Institute of Structural Analysis, Leibniz University Hannover, Appelstraße 9A, 30167 Hannover, Germany
[b] Department of Mechanical, Electrical, and Chemical Engineering, Oslo Metropolitan University, Pilestredet 35, 0166 Oslo, Norway
[c] Green Energy Lab, Department of Mechanical, Electrical and Chemical Engineering, OsloMet – Oslo Metropolitan University, Oslo, Norway
[d] Institute of Composite Structures and Adaptive Systems, DLR (German Aerospace Center), Lilienthalplatz 7, 38108 Brunswick, Niedersachsen, Germany

ARTICLE INFO

Keywords:
Polymer nanocomposites
Coarse-grained modeling
Machine learning optimization
Fracture properties
Nanoparticle agglomeration

ABSTRACT

Polymer nanocomposites, formed by incorporating nanoparticles into epoxy matrices, exhibit exceptional thermo-mechanical and fracture properties, making them ideal for advanced engineering applications. This study explores the enhancement of fracture properties of epoxies by nanoparticles and develops a coarse-grained (CG) model to enable this investigation. We present a novel artificial neural network (ANN)-assisted optimization framework to calibrate CG molecular simulation models. The algorithm integrates particle swarm optimization with ANN predictions, where ANN accelerates parameter optimization by minimizing errors between CG simulation results and all-atom reference data. This process significantly reduces computational cost while ensuring accurate predictions of critical properties, such as yield stress and elastic modulus, over a wide temperature range, demonstrating excellent temperature transferability of the model. Large-scale CG simulations facilitated the analysis of nanoparticle agglomeration effects on fracture behavior, a challenge infeasible for all-atom simulations. Simulation outcomes were qualitatively compared with experimental findings, offering valuable insights into the influence of nanoparticle distribution on fracture properties. This integrated approach provides a robust pathway for designing and optimizing polymer nanocomposites for real-world applications.

1. Introduction

Polymer nanocomposites (PNCs) have gained significant attention for their potential in environmental and engineering applications. Defined as polymer matrices with nano-fillers of at least one dimension smaller than 100 nm [1], PNCs offer exceptional thermo-mechanical properties that surpass those of individual components. Among commercially available nanofillers, boehmite nanoparticles (BNPs) are particularly suited for dispersing in epoxy resins to create lightweight structures for applications such as wind turbine rotor blades or structural components in aircraft and spacecraft. With their excellent thermo-mechanical properties, BNPs can significantly improve the characteristics of epoxy resins, even at low filler loadings [2].

However, BNPs often agglomerate during manufacturing, leading to poor dispersion within the polymer matrix and reducing their reinforcement efficiency [3]. Khorasani et al. [4] investigated the influence of BNPs on the thermomechanical properties of epoxy, finding that their presence not only improved thermal stability but also enhanced the nanomechanical properties of the resin. Specifically, the study reported increased hardness and modulus, indicating a stiffer, more durable epoxy matrix with BNPs. Jux et al. [5] demonstrated that BNPs significantly enhance the fracture toughness of epoxy resins, with the most substantial improvement observed at a filler content of 15 wt%. They found that a 15% BNP weight fraction increased the tensile modulus by 26% and the critical energy release rate by 62%. Arlt et al. [6] further explored the effects of taurine-modified BNPs, showing that incorporating 15 wt% of these modified nanoparticles resulted in a 25% increase in the elastic properties of carbon fiber/epoxy composites. Wu et al. [7] reported that BNP/epoxy nanocomposites with 4 wt% BNPs improved tensile strength and fracture toughness by 24.2% and 28.7%, respectively, over pure epoxy. Fankhänel et al. [8] used molecular dynamics simulations to show that strong BNP-polymer interactions alter chain packing, increase density, and restrict mobility near particles. These changes enhance the interphase, improving stiffness, strength, thermal stability, and stress transfer, leading to superior nanocomposite performance. Sangermano et al. [9] highlights the role of BNP dispersion and interfacial interactions in improving the thermal

* Corresponding author.
E-mail address: a.hente@isd.uni-hannover.de (A. Hente).

https://doi.org/10.1016/j.mtcomm.2025.113185
Received 14 March 2025; Received in revised form 14 June 2025; Accepted 23 June 2025
Available online 17 July 2025
2352-4928/© 2025 Institute of Structural Analysis, Leibniz University Hannover, Hannover, Germany. Published by Elsevier Ltd. This is an open access article under the CC BY license (http://creativecommons.org/licenses/by/4.0/).

and electrical insulation performance. These findings underscore the critical role of nanoparticle dispersion and interaction in optimizing the mechanical and fracture properties of polymer nanocomposites.

Due to the inherent complexity of nanomaterials, experimental tests alone often fail to fully elucidate their reinforcement mechanisms and effects on material failure. Polymer nanocomposites, which integrate nanoscale fillers within a polymer matrix, exhibit notable enhancements in mechanical and fracture properties, primarily because of unique molecular-level interactions between nanofillers and the polymer matrix. These nanofillers significantly influence fracture behavior by enhancing energy dissipation during crack initiation and propagation [10,11]. To gain deeper insights, researchers increasingly rely on molecular dynamics (MD) simulations, which allow precise observation of atomic-level interactions shaping composite behavior [12–15]. MD simulations by Li et al. [16] showed that Carbon nanotube/epoxy composites with a predefined crack exhibited gains of 24.8% in tensile strength and around 35% in energy release rate. Zhou et al. [17] provided a comprehensive review on PNCs reinforced with two-dimensional nanomaterials, discussing how variations in nanoparticle size, aspect ratio, and dispersion impact the mechanical and fracture properties of these composites. Hou et al. [18] further explored how the morphology of supra-molecular networks, modeled via MD simulations, influences the mechanical performance and self-healing behavior of PNCs, shedding light on their fracture resistance. Similarly, Hagita et al. [19] investigated the fracture behavior of PNCs with various fillers, revealing how filler type and distribution within the polymer matrix affect the fracture toughness. Roy et al. [20] focused on the inclusion of nanoparticles in polymer matrices, utilizing MD simulations to examine their impact on fracture toughness and material failure mechanisms at the atomic scale. Additionally, Arash et al. [21] introduced a complementary approach to study fracture mechanisms in viscoelastic polymer nanocomposites, capturing time-dependent deformation, exploring diverse loading scenarios, employing advanced modeling techniques, and providing insights into nanoparticle dispersion and interactions. Collectively, these studies highlight the critical role of MD simulations in studying nanoparticle characteristics, dispersion, and filler–matrix interactions to determine the fracture properties of polymer nanocomposites.

Despite their strengths, one primary challenge of all-atom simulations is the mismatch of time and length scales with experimental tests, making them computationally expensive and unsuitable for analyzing particle agglomeration effects on the mechanical and fracture behavior of nanocomposites. To address these limitations, CG simulations extend accessible time and length scales while preserving essential atomic details [22–24]. CG simulations simplify all-atom systems by representing groups of atoms as single superatoms, significantly reducing the degrees of freedom. Arash et al. [25] used a CG-based J-integral calculation to study fracture behavior in polymer nanocomposites. Cui et al. [26] explored how structural parameters influence the impact resistance of graphene-based nanocomposites, highlighting failure mechanisms like chain scission and disentanglement. Similarly, Hu et al. [27] investigated the effects of grafting density and chain length on fracture energy and void formation in polymer nanocomposites. Liu et al. [28] analyzed the mechanical and dynamic properties of nanocomposites with functionalized polymer chains, using simulations to reveal critical polymer-filler interactions that enhance mechanical performance and fracture toughness. Similarly, Arora et al. [29] employed coarse-grained simulations to study the effects of mechanical stress and structural inhomogeneities, such as chain length distribution and cross-link density, on the fracture behavior of polymer networks. Higuchi et al. [30] focused on double-network gels, using CG simulations to uncover how their unique structure resists crack propagation and enhances toughness. Moreover, Hu et al. [31] investigated dual cross-linked hydrogels, emphasizing the interplay between physical and chemical cross-links in energy dissipation and fracture behavior. Constructing accurate CG force fields, however, remains challenging, with traditional methods like the Martini force field [32], iterative Boltzmann inversion (IBI) [33,34], and strain energy conservation [35,36] providing calibration frameworks that face issues in convergence and structural specificity. These limitations highlight the need for improved approaches to achieve both accuracy and efficiency in CG modeling.

To further overcome computational challenges, optimization and neural network-based algorithms have been proposed to reduce costs and overcome challenges in convergence and recalibration, particularly for capturing temperature effects [37,38]. Bahtiri et al. [39,40] developed machine learning-based models, including a viscoelastic–viscoplastic and a physics-informed model, to enhance prediction accuracy for epoxy and short fiber/polymer nanocomposites under varied conditions. Hente et al. [41] introduced an optimization-assisted IBI method for calibrating temperature-transferable CG force fields. Bejagam et al. [42] combined all-atom simulations with particle swarm optimization (PSO) and ANN to expedite CG model development, and Duan et al. [43] extended this approach to model epoxies across broad temperature ranges and cross-linking degrees. Ruza et al. [44] introduced temperature-dependent graph neural network potentials to predict ionic liquid properties, while Lemke et al. [45] and Wang et al. [46] used neural networks to extract free energy surfaces and learn CG free energy functions, respectively. Loeffler et al. [47] proposed an active-learning workflow for training neural network force fields. Building on these methods, Loose et al. [48] demonstrated that equivariant neural networks enhance both accuracy and data efficiency in CG modeling, whereas Costa et al. [49] developed a hierarchical CG approach using SO(3)-equivariant autoencoders for scalable protein modeling. Furthermore, Yu et al. [50] introduced a graph neural network framework for identifying CG dynamical systems. Ricci et al. [51] focuses on enhancing CG simulations by incorporating machine learning algorithms to improve the accuracy and efficiency of modeling polymer systems. This integration facilitates efficient exploration of monomer sequence-structure–property relationships, aiding in the design of polymers with tailored properties while reducing computational costs and time.

The ongoing demand for efficient, robust algorithms to calibrate CG force fields with high accuracy and low computational cost remains a central challenge in nanocomposite modeling. This study addresses this by introducing an artificial neural network-based optimization approach that streamlines CG force field parameterization, significantly reducing computational time and improving accuracy compared to traditional methods like Martini, IBI, or strain energy conservation. Our CG force field accurately predicts properties like yield stress and elastic modulus across a wide temperature range, demonstrating strong temperature transferability. The primary novelty lies in integrating ANN-based optimization with CG simulations to overcome computational challenges, enhance force field accuracy, and ensure temperature transferability, resulting in a comprehensive CG model. Furthermore, our ANN-assisted optimization algorithm facilitates the development of a predictive CG model, enabling qualitative exploration of the impact of BNP agglomeration on the fracture properties of nanocomposites beyond the time and length scales accessible by all-atom simulations. This work investigates the relationship between fracture properties and the size of the volume element. It further examines the effects of BNP weight fraction, agglomerate size, and BNP distribution on the fracture behavior of BNP-reinforced polymers, supported by a combination of simulations and experimental validation.

2. All-atom simulations

In this study, all-atom simulations are conducted to obtain the thermo-mechanical properties of BNP/epoxy nanocomposites, which serve as target values for an ANN-assisted optimization procedure. The following sections explain the simulation details related to the curing process, glass transition temperature (Tg) predictions, and mechanical tests.

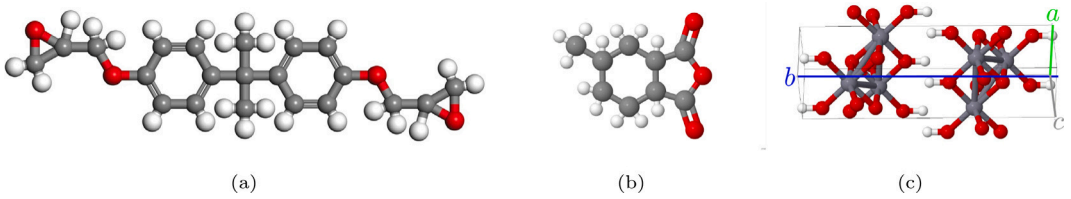

Fig. 1. Molecular structures of (a) a bisphenol-A-diglycidylether monomer, (b) a 4-methyl-1,2-cyclohexanedicarboxylic anhydride curing agent, and (c) the unit cell of the crystalline structure of boehmite (with lattice parameters a = 3.693, b = 12.221, and c = 2.865 Å). In (a) and (b), gray represents carbon, while in (c), it represents aluminum. Red and white indicate oxygen and hydrogen atoms, respectively. (For interpretation of the references to color in this figure legend, the reader is referred to the web version of this article.)

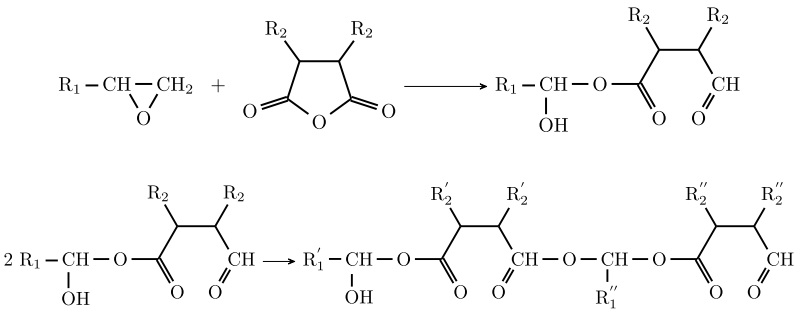

Fig. 2. Curing reaction mechanism between DGEBA epoxy and anhydride curing agent.

2.1. Materials

The curing simulations are performed for an epoxy resin consisting of bisphenol-A-diglycidylether (DGEBA) monomers and 4-methyl-1,2-cyclohexane dicarboxylic anhydride (MTHPA) hardeners. The molecular structure of DGEBA and the curing agent are shown in Figs. 1(a) and 1(b). The mixing ratio is the standard stoichiometric epoxy monomer/hardener mixing ratio of 100 : 90. The chemical reactions depicted in Fig. 2 involve the opening of the epoxide rings and the hydrolysis of the curing agent, enabling them to react with each other and generate carboxylic acids. These acids then react with the epoxy groups to produce hydroxyl groups, which further react with DGEBA and MTHPA.

As mentioned earlier, nanocomposite systems contain nano-scaled reinforcement materials to enhance mechanical properties. In this work, boehmite nanoparticles are added to our epoxy system. Boehmite, with the formula γ-AlO(OH), is an aluminum oxide hydroxide with lattice parameters a = 3.693, b = 12.221, and c = 2.865 Å. As illustrated in Fig. 1(c), central aluminum atoms are bonded to double layers of oxygen to form the crystalline structure of BNPs. The oxygen is bonded by hydrogen bonds to the hydroxyl groups of the octahedrons.

2.2. Cross-linking simulations

To obtain the material properties, the topology of the molecular network must realistically represent a cured epoxy system. For this purpose, DGEBA and hardener molecules are randomly placed in a periodic 60 × 60 × 60 $Å^3$ simulation box with an initial density of 1.2 g/cc. The selected box size represents the largest feasible dimension for MD simulations, ensuring that the RVE is adequately sized to capture the material's characteristics without exceeding computational resources [52]. The non-cross-linked models are generated using the open-source package PACKMOL [53]. Additionally, all-atom models of the BNP/epoxy systems contain one BNP nanoparticle centrally located. The boehmite structure consists of four layers with a thickness of 20 Å, as shown in Fig. 3. This thickness is selected as a compromise between computational feasibility and ensuring a realistic representation of nanoparticle dimensions. This size also allows the boehmite to interact effectively with the surrounding epoxy matrix while maintaining compatibility with the periodic boundary conditions.

For intermolecular interactions, the Dreiding force field [54] is utilized in all-atom simulations. Harmonic force fields govern all bond interactions, including stretching and bending potentials. Lennard-Jones potentials are used for the non-bond interactions between atoms with a cut-off distance of 12 Å. To obtain unlike pair potentials, the arithmetic mixing rule is applied [55]. The barostat [56] and Nosé–Hoover thermostat are used to control the system's pressure and temperature.

In the curing process of pure epoxy, epoxy monomers connect to an agent molecule, as explained in Section 2.1. This connection occurs through the formation of a methyl group on the monomer, which links to the hydroxyl group of the agent molecule. In the BNP/epoxy nanocomposite, the hydroxyl groups on the boehmite surface can also participate in the curing reaction [8].

For the cross-linking simulation of an uncured system, after energy minimization, the temperature is linearly increased to the curing temperature of 450 K [5]. An NPT ensemble for 1 ns and the constant pressure of 1 atm are used in the process. The following steps are then conducted for the cross-linking simulation:

1. A bond is formed between two reactive sites with the shortest possible length, with a cut-off of 4.5 Å for the reaction distance;
2. An equilibration is performed for a time period of 2.5 ps;

The cut-off distance of 4.5 Å represents the maximum distance at which reactive sites can form a bond, based on typical bond lengths and interaction distances observed in the chemical system. It balances realism and computational efficiency, avoiding unrealistic bonds with larger cut-offs and missed reactions with smaller ones. These two steps are repeated until the final degree of curing of around 90% is reached. Achieving 100% curing is often challenging in practice due to incomplete reactions and unreacted species. A 90% cure is not only more realistic but also reflects typical processing conditions. At this level, materials show significant mechanical property improvements while maintaining flexibility, striking an optimal balance between performance and processability. The time step during the simulation was 1 fs. The duration of each step and the cut-off value were selected to ensure a well-equilibrated system and sensible computing time. Due to the layered structure of the boehmite, the simulation box for nanocomposites is simulated using an isoenthalpic–isobaric ensemble (NPH) with a Nosé–Hoover barostat [56] and an additional Langevin

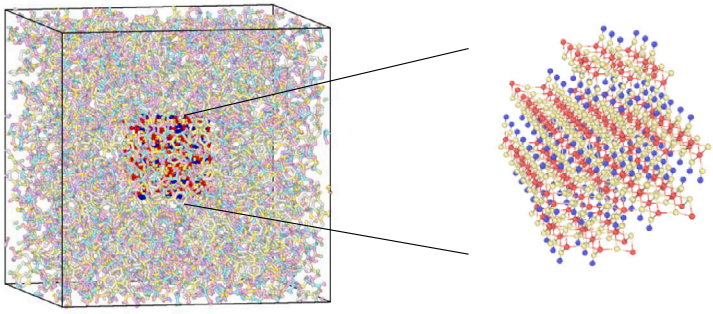

(a) (b)

Fig. 3. A simulation box of cured boehmite/epoxy nanocomposites with dimensions of 60 × 60 × 60 Å^3 for the all-atom model, and (b) a four-layer boehmite structure with a thickness of 20 Å.

thermostat [57], instead of an NPT ensemble. The curing process is conducted using the Large-scale Atomic/Molecular Massively Parallel Simulator (LAMMPS) [58] with our modification to the fix bond/create command. This command calculates the distances between all possible reaction groups and forms a bond with the smallest reaction distance, discarding all reaction distances larger than the chosen cut-off. Additionally, for visualization and analysis of the data, OVITO [59] is used in this work.

2.3. Tensile simulations and Tg predictions

After cross-linking, the cured system is cooled down to room temperature and then relaxed using an NPT ensemble for 1.5 ns. To obtain the stress–strain relationship, tensile deformation is applied to the systems by increasing the box length in the tensile direction and remapping the atom coordinates at every step. To allow for natural Poisson contraction, stresses perpendicular to the tensile direction are fixed at zero. The time step for a constant strain rate of $\dot{\epsilon} = 10^9$ 1/s is set to 0.02 fs. To obtain an average stress–strain response, tensile simulations are repeated in the X, Y, and Z directions for five different configurations. Fig. 4(b) shows the average stress–strain curve.

A piecewise cubic spline interpolation is fitted to the simulation data points to extract the yield stress, considering an optimized knot. The position of each knot is optimized by minimizing the least square error between the fit curve and the data points. The yield point is identified as the first maximum of the spline fit, where the derivative of stress with respect to strain is zero. Furthermore, to extract the relationship between specific volume ($1/\rho$) and temperature for calculating Tg, the temperature of an equilibrated system is linearly increased from 200 K to 600 K. Fig. 4(a) shows the variation of specific volume versus temperature, measured based on the average of simulation results for five different configurations. The glass transition temperature T_g = 433.15 K, predicted using all-atom simulations, is consistent with the experimental value of 426.15 K reported in the literature [4].

3. Coarse-grained modeling

3.1. Mapping scheme

In coarse-grained models, a set of atoms is mapped into a CG super-atom (bead). Therefore, the first step in coarse-graining is to define proper mapping schemes. CG beads must enable the model to maintain the underlying chemistry. Mapping schemes are based on the chemical compositions of molecules and the repeating units of the monomers [60]. In this work, the highest achievable level of coarse-graining is adopted based on the research work of Hente et al. [41].

Each monomer is mapped into one bead in the epoxy mapping scheme, as illustrated in Figs. 5(a) and 5(b). Accordingly, the CG system comprises two types of beads: one for the bisphenol-A monomer, named A, and one for the hardener, named B. The atomic masses of beads A and B are 340.4128 amu and 166.1739 amu, respectively. In this scenario, the degrees of freedom (DOF) for beads A and B decrease by factors of 49 and 22, respectively. For a box size of 60 × 60 × 60 Å^3, filled with the epoxy system, the number of beads decreases by approximately 32 times for the CG model compared to the full atomistic model.

Boehmite is a mineral composed of aluminum with a bulk modulus of 93 GPa [61]. Its structural properties have been studied experimentally using XRD [62] and Raman spectroscopy [63], as well as numerically using quantum mechanics [61]. The ultra-high elastic modulus of BNPs, compared to the epoxy matrix, allows us to model them as rigid particles in CG modeling. In the subsequent simulations, one primary particle with a length of 20 Å is mapped to a single CG bead, named P. Compared to its full atomistic system, the DOF in this CG model decrease by 656 times. The atomic mass of P is 10,433 amu. The primary particle is illustrated in Fig. 5(c).

3.2. Coarse-grained force field

After the mapping scheme, a CG force field should be calibrated to simulate BNP/epoxy nanocomposites and predict their thermo-mechanical properties. The potential energy function of a CG force field is decomposed into bond and non-bond terms. The total potential energy of a system is then given by

$$E_{total}(d,\theta,r) = \sum_i E_{b_i} + \sum_j E_{a_j} + \sum_k E_{nonb_k}, \tag{1}$$

where E_b, E_a are the energy terms corresponding to variations in bond length and bond angle, respectively, and E_{nonb} represents the non-bond interactions. It is worth noting that terms corresponding to torsional interactions are omitted due to their minor effects.

To consider bond breakage, the Morse potential [54] is used in this CG model for stretching:

$$E_b(l) = D_b(1 - e^{-\alpha(r-r_0)})^2, \tag{2}$$

where r_0 represents the equilibrium bond distance, D_b is the depth of the potential well, and α shows a stiffness parameter. Considering the bond between epoxy and BNPs [8], there are two types of bonds in our nanocomposite system, AB and PB.

The harmonic force field is applied for the bending potential in this CG model:

$$E_a(\theta) = \frac{K_\theta}{2}(\theta - \theta_0)^2, \tag{3}$$

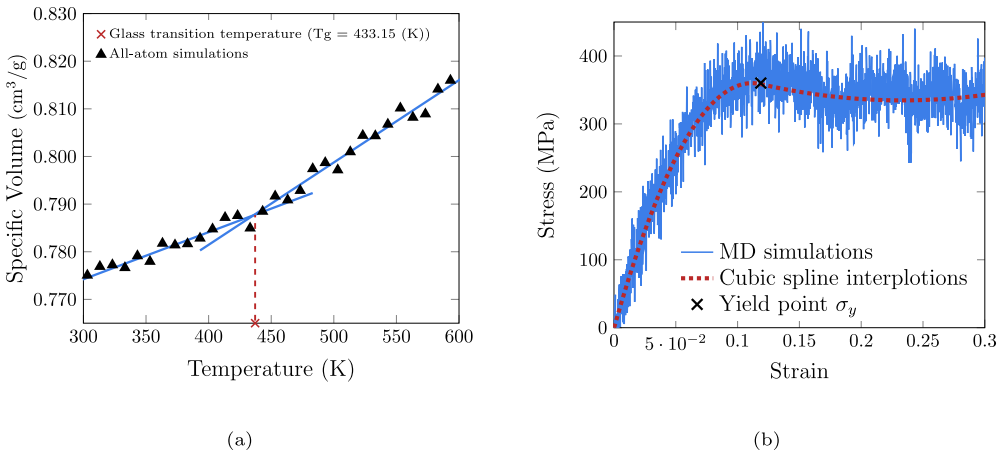

Fig. 4. (a) Average specific volume–temperature curve and (b) average stress–strain curve for pure epoxy, obtained from all-atom simulations.

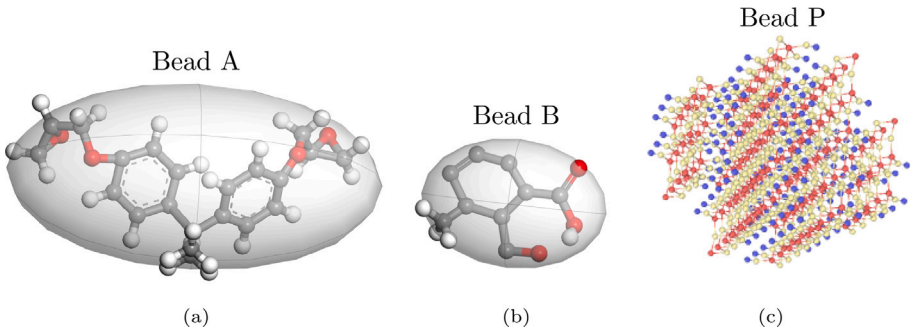

Fig. 5. All-atom model illustrations of (a) a DGEBA epoxy, (b) a curing agent, and (c) a four-layer boehmite structure with a thickness of 20 Å. Each is represented by a corresponding CG bead.

where K_θ and θ_0 represent the spring constant and the equilibrium angle, respectively. In the CG model, there are two types of angles: BAB and PBP.

The non-bond interactions are modeled using a Lennard-Jones-(12,6) potential with a cut-off distance of 20 Å,

$$E_{vdW}(r) = \epsilon \left[(\frac{\sigma}{r})^{12} - (\frac{\sigma}{r})^{6} \right], \tag{4}$$

where ϵ represents the equilibrium well depth and σ the equilibrium distance. Since there are three CG types, the CG model of nanocomposites includes six total unknown non-bond force fields: ϵ^{AA}, ϵ^{BB}, ϵ^{PP}, σ^{AA}, σ^{BB}, σ^{PP}. For unlike bead pairs, the arithmetic mixing rule [55] is used to obtain pair potentials, where the Lennard-Jones (LJ) parameters are determined as follows: $\epsilon_{ij} = \sqrt{\epsilon_i \epsilon_j}$ and $\sigma_{ij} = \frac{1}{2}(\sigma_i + \sigma_j)$.

The CG force field is utilized to predict the thermo-mechanical properties of BNP/epoxy nanocomposites. The preparation of the non-cross-linked system and the curing process mirror those used in all-atom simulations. Initially, monomer and hardener molecules are generated and randomly distributed within a simulation box. Morse potentials are employed for bond interactions, while harmonic potentials manage bending interactions. Before initiating the cross-linking simulation, the simulation box undergoes energy minimization. Similar steps are followed for the cross-linking of an uncured system, treated as a molecular system. In CG simulations, a reaction distance cutoff of 10 Å is applied. The final degree of curing reaches approximately 90%. The durations of the individual steps and the chosen cut-off value are carefully selected to ensure the system is well-equilibrated within a reasonable computing time.

3.3. Machine-learning assisted optimization

In this study, an ANN-assisted optimization algorithm is proposed to calibrate CG force fields for BNP/epoxy nanocomposites. The suggested algorithm represented in Table 1, includes CG simulations and a combination of an ANN algorithm and PSO. This approach aims to accelerate the search process in finding the optimal solution. In the ANN-assisted CG model optimization, each particle represents a set of unknown CG force field parameters that define the interactions in the system. These parameters are optimized to match the thermo-mechanical properties of the CG model to those obtained from all-atom simulations. The inputs to the ANN are the force field parameters, including bond and angle constants, equilibrium values, and van der Waals parameters (e.g. D_b, α, r_0, K_θ, θ_0, σ, and ϵ). The outputs of the ANN are the corresponding thermo-mechanical properties derived from CG simulations, such as mass density, Young's modulus, glass transition temperature, and yield stress.

3.3.1. MLP training

The true advantage of neural networks lies in their ability to represent both linear and nonlinear relationships derived directly from data processing. A multilayer perceptron (MLP) is a representation of nonlinear connections between sets of input data and a set of outputs [64]. A typical MLP structure is composed of interconnected nodes in multiple layers, where the outputs of each node are processed through a nonlinear activation function. The output activation $a^{(l+1)}$ at layer $l+1$ is derived from the input activation $a^{(l)}$ [65],

$$a^{(l+1)} = \sigma(W^{(l)} a^{(l)} + b^{(l)}), \tag{5}$$

Table 1
ANN-assisted optimization algorithm for calibrating CG force fields.

1. Generate particles with random swarm positions and velocities
2. Evaluate the fitness of the swarm, and find the individual and global best of the swarm
3. Update the velocity and position of each particle using a simulation-trained ANN model
4. Update the inertia weight and check for termination criterion
5. **if** $f \leq$ tolerance (see Eq. (11)) **then**
   return the optimized CG force field
   else
   go to step 2
   end if

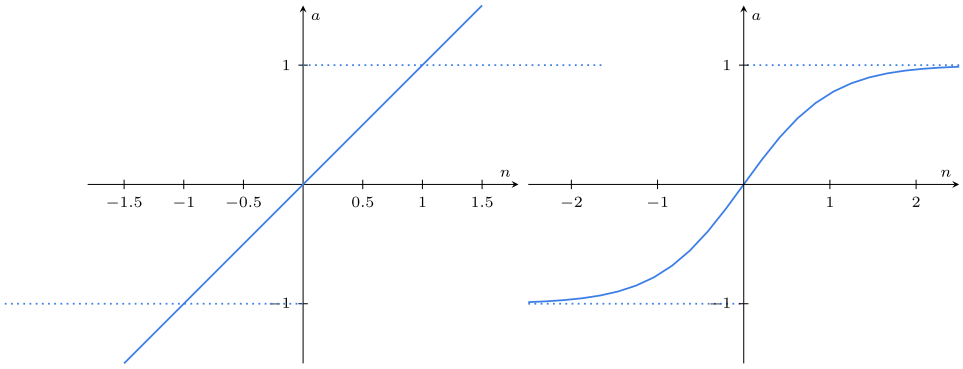

(a) a = purelin(n) (b) a = tansig(n)

Fig. 6. Transfer functions for (a) the linear function and (b) the hyperbolic tangent function.

where l stands for a specific layer, $W^{(l)}$ and $b^{(l)}$ represent the weight and bias at layer l and σ denotes the nonlinear activation function. The activation functions for the input and output layers are the identity function, as shown in Fig. 6(a). For the hidden layers, the hyperbolic tangent function, which is a nonlinear activation function, is used (see Fig. 6(b)).

In the case of an m-layer multilayer perceptron, the last output layer is defined as,

$$h_{W,b}(x) = a^{(m)}, \tag{6}$$

while the first input layer is represented by $a^{(1)} = x$. The weights W and bias b are trained using a local optimization method from the Levenberg–Marquardt algorithm [66],

$$\mathbf{J}_{new} = \mathbf{J}_{old} - (\mathbf{J}^T\mathbf{J} + \mu\mathbf{I})^{-1}\mathbf{J}^T\mathbf{e}, \tag{7}$$

where $\mathbf{J}$ represents the Jacobian and $\mathbf{I}$ stands for the identity matrix, respectively. The error vector in this equation is denoted by $\mathbf{e}$. The objective function is designed to minimize the difference between the predicted and the desired outputs,

$$J(W, b; x, y) = \frac{1}{2}\left\|h_{W,b}(x) - y\right\|^2. \tag{8}$$

Eqs. (8)–(11) and Fig. 6 represent standard neural network formulations, included for completeness and to support readers who may be less familiar with these techniques. Here, the force field parameters are optimized using an ANN surrogate, as shown in Fig. 7(a). To gather the comprehensive results required for training the ANN model, the epoxy system under various thermo-mechanical loadings is first simulated using the CG model with different force field parameters. These simulations facilitate the collection of data on the corresponding thermo-mechanical properties of the epoxy, including mass density, Young's modulus, glass transition temperature, and yield stress. To mitigate noise from randomly cross-linked polymer networks and thermal fluctuations, the simulation results from each test are averaged over nine different molecular configurations and compiled into a dataset. If a simulation result deviates from others by more than 50%, it is considered an outlier resulting from an unrealistic molecular structure and is excluded from the dataset. Consequently, the distribution of thermo-mechanical properties relative to the force field parameters is obtained. The output parameters of the ANN algorithm — density, Young's modulus, glass transition temperature, and yield stress — are computed from CG simulations of the pure epoxy system. The force field parameters, including D_b^{AB}, α^{AB}, r_0^{AB}, K_θ^{BAB}, θ_0^{BAB}, σ^{AA}, σ^{BB}, ϵ^{AA} and ϵ^{BB}, are selected as input data for a MLP, a type of feedforward ANN.

We optimize all force field parameters, including equilibrium bond distances and angles, using an ANN to enhance the adaptability and accuracy of our CG model across diverse simulation conditions. This method facilitates flexible parameterization and the discovery of non-intuitive relationships that static extraction methods might miss. Although this approach increases complexity and could lead to multiple viable parameters sets, it prevents overfitting to specific all-atom simulations and ensures broader applicability. By incorporating constraints within the ANN assisted optimization, we keep parameters within physically plausible ranges, addressing concerns about their physical meaningfulness. Additionally, comparative validation studies, as shown in the author's previous paper [41], confirm the effectiveness and accuracy of these parameters against traditional methods like the inverse Boltzmann method, which was insufficiently robust for this study. While constitutive equations provide physical interpretability, the complexity of nanoparticle-reinforced polymers — particularly dispersion and agglomeration effects — challenges their derivation without simplifications. The ANN approach was selected for its ability to model these behaviors directly from data, facilitating efficient CG force field optimization.

Based on the dataset, the MLP is trained to establish a representation of the data relations. The dataset randomly divides into training, validation, and testing data. The datasets are generated as follows: a training set with 3600 configurations, a validation set containing 200 configurations, and a test set with 200 configurations to evaluate the performance of the model. The 4000 configurations refer to unique sets of CG force field parameters varied systematically, with each set used in LAMMPS-based CG simulations to compute thermo-mechanical properties for MLP training. The parameters are sampled using the Halton sequence algorithm [67] to ensure uniform parameter space

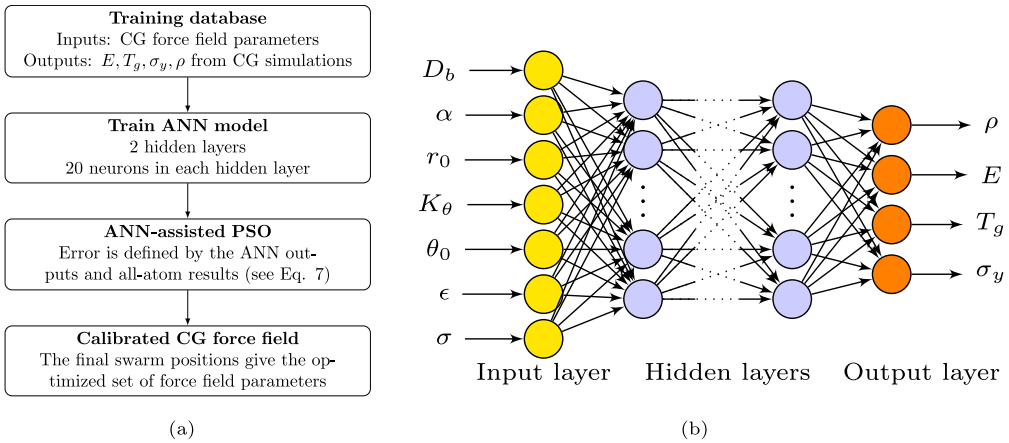

Fig. 7. (a) A schematic illustration of the CG force field parameterization and (b) the ANN surrogate with one input layer, one output layer, and two hidden layers.

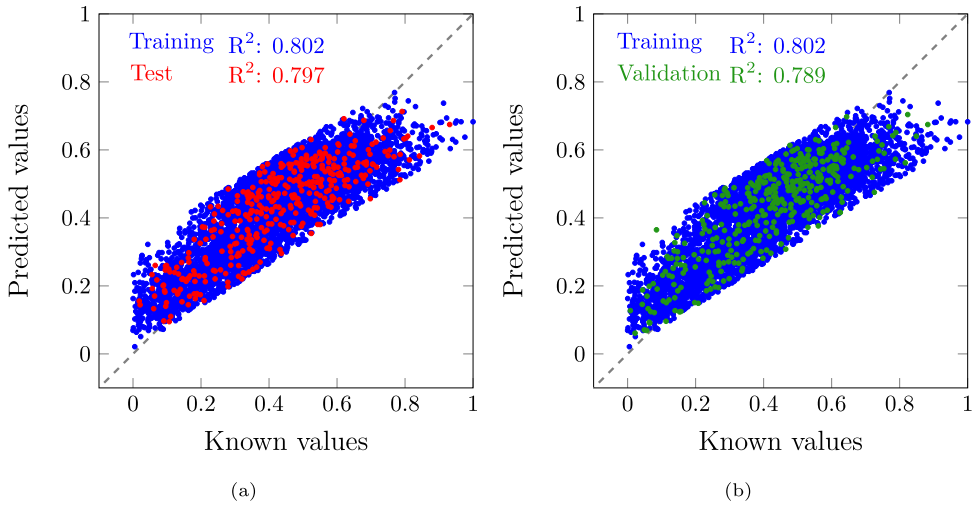

Fig. 8. Performance of the ANN model for (a) training and testing, and (b) training and validation. Known values in x-axis refer to target thermo-mechanical properties from All-atom Simulations (Density, Young's Modulus, T_g, Yield Stress). Each data point represents a prediction for one of these four properties across the dataset (3600 training, 200 validation, and 200 testing configurations).

coverage. The topology of the model, which includes an input layer, two hidden layers, and one output layer, is represented in Fig. 7(b). Each hidden layer contains 20 neurons, and the hyperbolic tangent function is used as the activation function for neurons in the hidden layers. Our simulations suggest that this configuration of hidden layers and neurons provides sufficient prediction accuracy. It is worth noting that the chosen architecture adequately addresses the problem, as empirical evidence from model evaluation (training and validation loss curves) supports this choice. The architecture strikes the right balance between model complexity and the problem's requirements while avoiding potential overfitting, which is the model's failure to generalize from the training data to new data. Input and output data were normalized to [0, 1] using min–max scaling, with bounds derived from the dataset's extrema, ensuring uniform scaling across diverse physical properties.

Here, The Levenberg–Marquardt algorithm is utilized to perform regression and optimize the weights of the ANN model. Performance is evaluated using a loss function based on the mean squared error (MSE). To enhance the MLP's generalization capacity, both input and output data are normalized within the range of 0 to 1. The entire learning process is conducted in MATLAB using the Neural Network Toolbox. The regressions predicted by the ANN model for both training and test data are shown in Fig. 8. For CG models, achieving high predictive accuracy means effectively balancing accuracy with computational efficiency. An R^2 of 0.8 suggests that the ANN captures a significant portion of the necessary dynamics, generally satisfactory for many coarse-grained simulations [68–70]. The consistent R^2 values across training, testing, and validation indicate that the model generalizes well to different datasets—a crucial aspect for CG modeling, as the force fields must perform reliably under various conditions. In the field of computational chemistry and molecular dynamics, this ANN model shows robust performance and generalizes well without significant overfitting. This level of performance is adequate for many practical applications, including ours, as future validation will demonstrate in the following sections. It is worth noting that the MLP's R^2 of 0.8 reflects a balanced trade-off in predicting multiple properties, achieved through normalization and a summed error objective function, ensuring adequate accuracy for CG applications without overfitting to any single property.

Fig. 9 presents the property-specific performance of our ANN model, revealing significant variations in predictive accuracy across different thermo-mechanical properties. The model achieves excellent performance for density predictions (R^2 = 0.87), reflecting the direct correlation between molecular packing and basic force field parameters. Young's Modulus (R^2 = 0.84) also demonstrates strong performance while yield Stress (R^2 = 0.74) and glass transition temperature (R^2 = 0.72) show reasonable accuracy. The consistent gap between training and testing performance (typically 2%–7% lower R^2 for test data) indicates good model generalization without significant overfitting. The

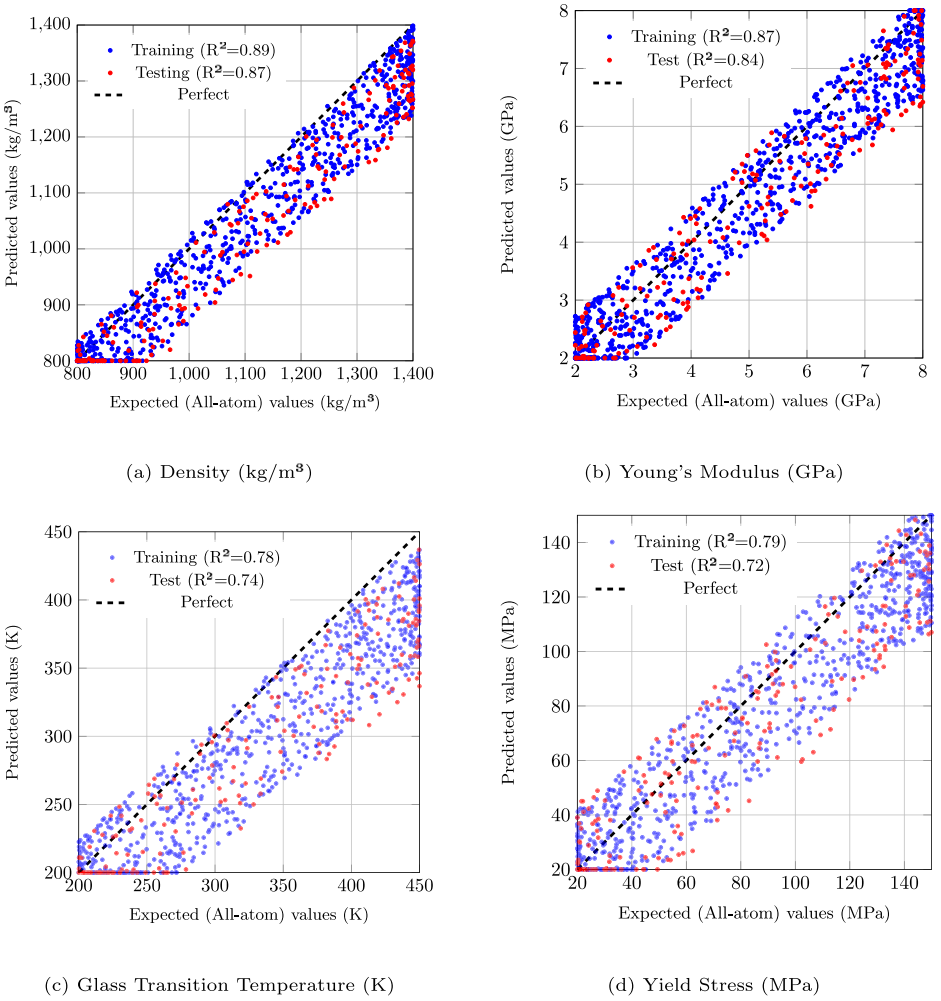

(a) Density (kg/m³) (b) Young's Modulus (GPa)

(c) Glass Transition Temperature (K) (d) Yield Stress (MPa)

Fig. 9. Individual ANN model performance for predicting thermo-mechanical properties from CG force field parameters: (a) Density, (b) Young's Modulus, (c) Glass transition temperature, and (d) Yield stress. Each subplot shows predictions vs. target values from all-atom simulations, with separate R^2 values revealing property-specific model performance.

overall average R^2 of 0.80 across all properties demonstrates that the MLP provides reliable predictions while highlighting which properties can be predicted with higher confidence for practical applications.

Fig. 10 shows the MSE versus epoch for training (3600 configurations), validation (200 configurations) and test (200 configurations) sets. The plot demonstrates a steady decrease in training loss, confirming effective learning of the thermo-mechanical property mappings. In addition, it shows a corresponding decrease in validation loss, plateauing near the tolerance of 0.01, indicating no significant overfitting. Fig. 10 presents the training and validation loss versus epoch, illustrating convergence of the MLP model and its ability to generalize across the dataset.

3.3.2. PSO optimization

We chose PSO for its suitability in optimizing continuous force field parameters. It provides fast convergence, balances exploration and refinement efficiently, minimizes computational overhead, and scales well with parallel simulations. In the PSO algorithm, the swarm moves across the grid search space as defined by [71],

$$\mathbf{X}^i_{j+1} = \mathbf{X}^i_j + \mathbf{V}^i_{j+1}, \tag{9}$$

$$\mathbf{V}^i_{j+1} = \eta \mathbf{V}^i_j + c_1 r^i_{1j}(\mathbf{P}^{i-best}_j - \mathbf{X}^i_j) + c_2 r^i_{2j}(\mathbf{P}^{g-best}_j - \mathbf{X}^i_j), \tag{10}$$

where $\mathbf{V}^i_j$ and $\mathbf{X}^i_j$ denote the velocity and position of the ith particle at the jth iteration, respectively. $\mathbf{P}^{i-best}_j$ and $\mathbf{P}^{g-best}_j$ represent the individual best and the global best positions of the swarm, respectively.

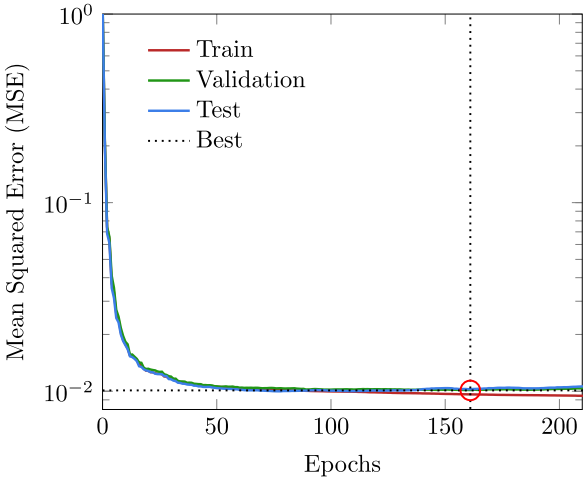

Fig. 10. The MSE versus epoch for training (3600 configurations), validation (200 configurations) and test (200 configurations) sets. Best validation performance is 0.01 at epoch 161.

Coefficients c_1 and c_2 are the constants; η is the inertia factor. r^i_{1j} and r^i_{2j} are random parameters within the range of 0 to 1.

Table 2
Search space for CG force field parameters used in the optimization process.

Type of interactions	Parameters	Initial guess range	Optimization boundaries
Bond	D_b (kcal/mol/Å^2)	40–100	10–150
	α (–)	~ 1	
	r_0 (Å)	5–12	2–20
Angle	K_θ (kcal/mol/rad^2)	20–100	10–200
	θ_0 (°)	~ 150	
vdW	ϵ (kcal/mol)	4–100	> 0
	σ (Å)	7–16	> 0

We employ the ANN model to generate "good particles" during each PSO iteration, which aids in accelerating the search process for the optimal solution. These particles are closer to the best solution compared to other searched positions. The PSO particle with the greatest fitness is replaced by the new particle predicted by the ANN model. Consequently, all PSO particles are updated based on this new particle. The swarm size used in the PSO optimization algorithm is set to 10 particles, with each particle representing the unknown CG force field parameters.

To determine the specific size of the search space initially, as mentioned earlier, an empirical approach is informed by physical intuition and preliminary parametric studies. Specifically, for the Morse bond potential parameters, the equilibrium bond distance (r_0) was initialized based on average bond lengths from all-atom simulations of the BNP/epoxy system, typically ranging from 5 to 12 Å depending on the bead pair (e.g., AB or PB bonds). The potential well depth (D_b) was set between 40 and 100 kcal/mol, reflecting typical bond energies in polymers, while the stiffness parameter (α) was initialized around 1.0, consistent with similar materials. For the harmonic angle potential, the spring constant (K_θ) was set between 20 and 100 kcal/mol/rad^2, and the equilibrium angle (θ_0) near 150°, in line with epoxy chain geometry. Lennard-Jones parameters were initialized with ϵ values between 4 and 100 kcal/mol and σ between 7 and 16 Å, based on van der Waals interactions observed in all-atom data. To ensure physical realism during PSO optimization, parameter bounds were applied. Bond lengths (r_0) were restricted to 2–20 Å, and force constants (D_b, K_θ) were limited to 10–150 kcal/mol and 10–200 kcal/mol/rad^2, respectively. LJ parameters were constrained to positive values with upper limits set to avoid unphysical energy scales or atomic overlaps. To provide a clear visual reference Table 2 has been prepared.

In the optimization procedure, the total error is defined using the thermo-mechanical properties obtained from CG simulation-trained ANN models and all-atom simulations,

$$f = \sum_{i=1}^{N} \left(\frac{F_i^{ANN}(\mathbf{X})}{F_i^{ref}} - 1 \right)^2, \tag{11}$$

where $F_i^{ref} (i = 1, 2, \ldots, N)$ represents a set of known properties from all-atom simulations, and $F_i^{ANN}(\mathbf{X})$ is the same set calculated by the CG simulation-trained ANN model using the unknown force field parameters $\mathbf{X} = [D_b, \alpha, r_0, K_\theta, \theta_0, \epsilon, \sigma]$. The iteration continues until the objective function is reduced to a specified tolerance. The target values used in the procedure are the mass density, Young's modulus, glass transition temperature and yield stress from the all-atom simulations. To balance high accuracy and low computational cost, the tolerance is set at 0.01. It is worth noting that using yield stress instead of the full stress–strain curve simplifies the optimization process by reducing complexity, as it represents a single scalar value rather than a comprehensive dataset. Yield stress is a critical mechanical indicator, capturing the onset of plastic deformation, which is often sufficient for many applications. This approach also reduces computational costs by eliminating the need to simulate the entire stress–strain response. While optimizing yield stress alone may not be as robust as analyzing the full curve, it is a practical and efficient metric, particularly as it is one of the four thermomechanical properties considered in this study.

Table 3
Optimized CG force field parameters.

Type of interactions	Parameters	Epoxy	BNP
Bond	D_b (kcal/mol/Å^2)	45.86	95.81
	α (–)	0.97	0.98
	r_0 (Å)	5.04	12.05
Angle	K_θ (kcal/mol/rad^2)	25.07	98.23
	θ_0 (°)	149.74	150.98
vdW	ϵ (kcal/mol)	4.53, 4.47	100.64
	σ (Å)	7.94, 7.78	16.19

The trained network will significantly accelerate the calculation of thermo-mechanical properties derived from a set of force field parameters. This model can be utilized to optimize these parameters by minimizing the differences between the thermo-mechanical properties obtained from the CG simulation-trained ANN model and those from the all-atom simulations. The use of the ANN model significantly reduced the computational time required for the optimization process, achieving a reduction by an order of magnitude compared to pure optimization alone. With ANN assistance, the optimization process becomes far more efficient, enabling faster convergence and facilitating a broader exploration of the design space. The reason we employ optimization is to reduce computational effort. One example that highlights the differences is the work by Wang et al. [46], who demonstrated that a deep learning approach for CG-MD can achieve high accuracy in capturing multi-body interactions for systems such as alanine dipeptide and Chignolin. However, this level of accuracy comes at the cost of requiring extensive training data. For alanine dipeptide, their model was trained on 1 million configurations derived from a 1-microsecond all-atom simulation in explicit solvent, with coordinates and forces saved every picosecond. For Chignolin, the training dataset comprised 3742 short MD simulations, each 50 nanoseconds long, resulting in a total simulation time of 187.2 microseconds. These large datasets underscore the data-intensive nature of MLFFs compared to the ANN-assisted approach in our study, which utilizes a more modest dataset of 4000 configurations to achieve sufficient accuracy for CG parameter optimization.

After optimizing the CG force field for the epoxy system, the same ANN-assisted optimization procedure is applied to calibrate the force field parameters related to BNP nanoparticles. In this case, the inputs to the ANN model are D_b^{PB}, α^{PB}, r_0^{PB}, K_θ^{BPB}, θ_0^{BPB}, ϵ^{PP}, and σ^{PP}. Additionally, the normalized mass density, Young's modulus, glass transition temperature, and yield stress computed using CG simulations of a single BNP/epoxy system serve as the output values. The design of the ANN model is identical to that used for the pure epoxy. The optimal solutions searched for the force fields of the CG model are listed in Table 3.

4. Experiments

4.1. Manufacturing

Manufacturing BNP/Epoxy test specimens can be divided into four sections: dispersing, mixing, curing, and chipping. The aim of dispersing is to comminute and homogenize BNP in the epoxy resin. To achieve

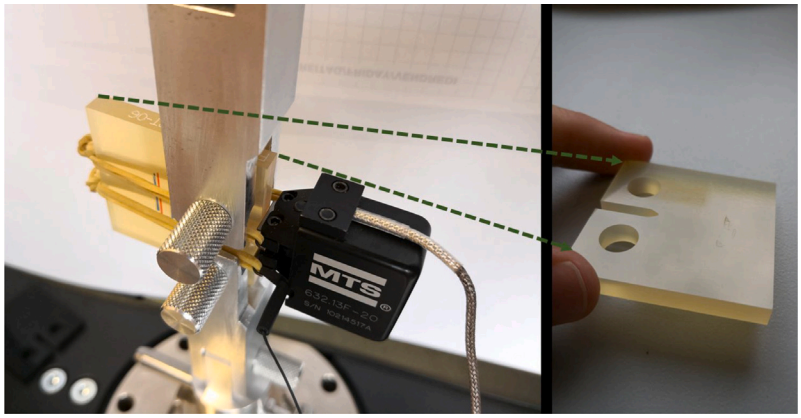

Fig. 11. Fracture test device with a single nanocomposite test specimen.

the best results, it is essential to attain a high particle fraction (30 wt%). As a result, the suspensions become highly viscous, which facilitates the effective transmission of shear forces necessary for dispersing. Dispersing was performed using both a kneader and a three-roll mill. The quality of dispersion was verified by dynamic light scattering methods, analogous to those described in [3]. Since BNP can interact with epoxy, the dispersions are stored at low temperatures (−20 °C) to prevent pre-cross-linking. After dispersing, curing agents are added during the mixing process with a ratio of 100:90:1 (epoxy:hardener). Mixing was carried out using a vacuum centrifugal mixer at rotational speeds up to 2100 rpm, with simultaneous degassing, leading to high-quality mixtures. For curing, the mixtures are cast into pre-heated molds and cured for 4 hours at 80 °C for gelation and an additional 4 hours at 120 °C for post-curing. In the final step, the cured test plates are milled into test specimens according to ISO 13586.

4.2. Mechanical tests

To make the experimental results statistically robust, 10 different compact-tension (CT) specimens are used for the fracture tests. All fracture specimens are produced and tested according to ISO 13586, as shown in Fig. 11. The specimens were kept under constant conditions for at least two days at a temperature of 23 °C and humidity of 51%. The test speed is set at 10 mm/min. The cross-head displacement and arising forces during the fracture testing are recorded. The specimens are pre-notched with lengths ranging from 7 to 13 mm. The mode I stress intensity factor, K_I, is then measured using the force–displacement curves obtained from the CT tests. Furthermore, the effects of BNP content on the fracture properties were studied using a standardized test configuration, with BNP weight fractions varying from 0 to 15 wt%.

5. Results and discussion

5.1. Experimental results

The fracture behavior of BNP/epoxy composites is investigated using CT tests, as described in Section 4. Accordingly, the mode I stress intensity factor for the BNP/epoxy nanocomposites is measured. The stress intensity factor for the CT specimen, illustrated in Fig. 12(a), is given by [72]:

$$K_I = \frac{P}{B\sqrt{W}} \frac{2+\frac{a}{W}}{(1-\frac{a}{W})^{\frac{3}{2}}} [0.886 + 4.64(\frac{a}{W}) - 13.32(\frac{a}{W})^2 + 14.72(\frac{a}{W})^3 - 5.60(\frac{a}{W})^4], \quad (12)$$

Table 4
Mode I stress intensity factor for BNP/epoxy nanocomposites at varying BNP weight fractions.

wt%	0	1	2.5	5	10	15
K_I (kPa$\sqrt{\text{m}}$)	502 ± 11	559 ± 8	564 ± 10	598 ± 11	641 ± 8	702 ± 12

where $W = 35$ mm and $B = 5$ mm represent the width and thickness of the specimen, respectively; $a = 16$ mm is the initial crack length, and P is the maximum force obtained from the force–displacement response.

The force–displacement curves obtained for BNP/epoxy specimens with different BNP weight fractions are shown in Fig. 12(b). Using the force–displacement responses and Eq. (12), K_I can be measured, and the results are listed in Table 4. According to the experimental data, increasing the particle content leads to a significant increase in K_I. For example, 15 wt% BNP increases K_I by around 39% compared to pure epoxy.

5.2. Numerical verification of the ANN-calibrated CG model

Verifying a CG model is crucial to prevent inaccuracies from simplifications, ensuring their effective use in academic and industrial applications. Initially, a simulation box size of 60 × 60 × 60 Å^3 with periodic boundary conditions is constructed, containing 21,374 atoms. Another box of the same size is also constructed, featuring a primary particle with an average diameter of 20 Å in the center, containing 21,095 atoms, representing a 6 wt% nanoparticle weight fraction. The epoxy molecules are randomly placed in the box, with periodic boundary conditions applied in all directions. The simulation box of the cured BNP/epoxy nanocomposites for the all-atom model can be seen in Fig. 13(a). The system is then cured as described in Section 2.2, and the steps are repeated to generate three unique all-atom configurations. The mass density of the system is 1.2 $\frac{g}{cc}$. All-atom simulations are conducted using the Dreiding force field with a harmonic bond potential and a LJ potential for non-bond interactions, with a non-bond cut-off distance set at 12 Å. For all-atom simulations of the BNP/epoxy nanocomposite, the timestep for the curing process is reduced to 0.1 fs due to the crystalline structure of the particles. An NPH with an additional Langevin thermostat [57] is used to relax the system.

The CG models are then constructed according to the mapping schemes introduced in Section 3.1. The simulation box for pure epoxy contains 677 beads. In the case of the nanocomposite, the box includes 668 epoxy beads and one boehmite bead. The mass density of the CG models is set at $\rho = 1.2$ $\frac{g}{cc}$. The simulation box of the cured BNP/epoxy nanocomposites used for the CG model is illustrated in Fig. 13(b). In the CG simulations, Morse and harmonic potentials are used for bond and

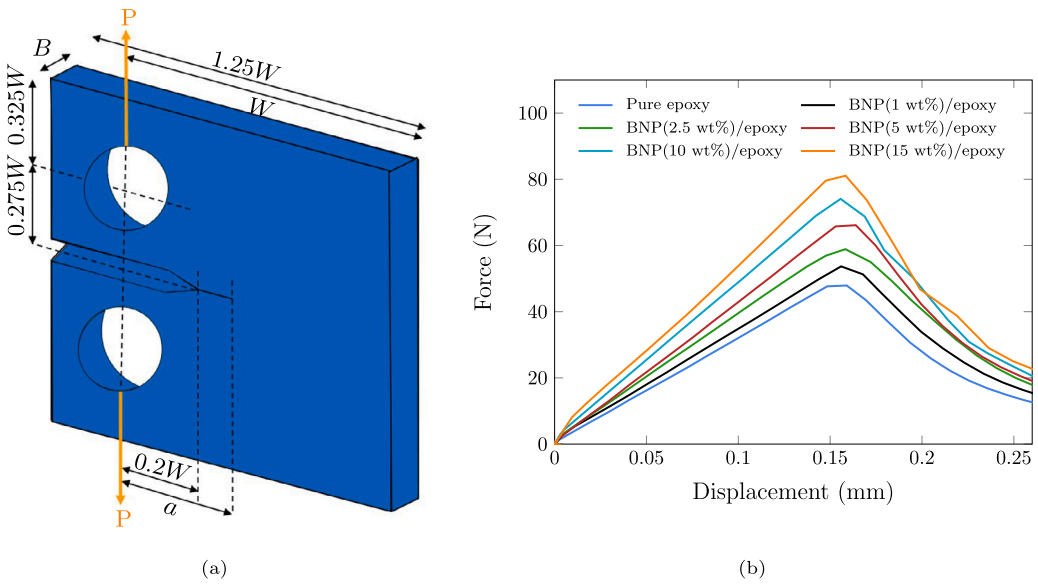

Fig. 12. (a) Schematic illustration of the compact-tension specimen and (b) the effect of BNP weight fraction on the force–displacement response.

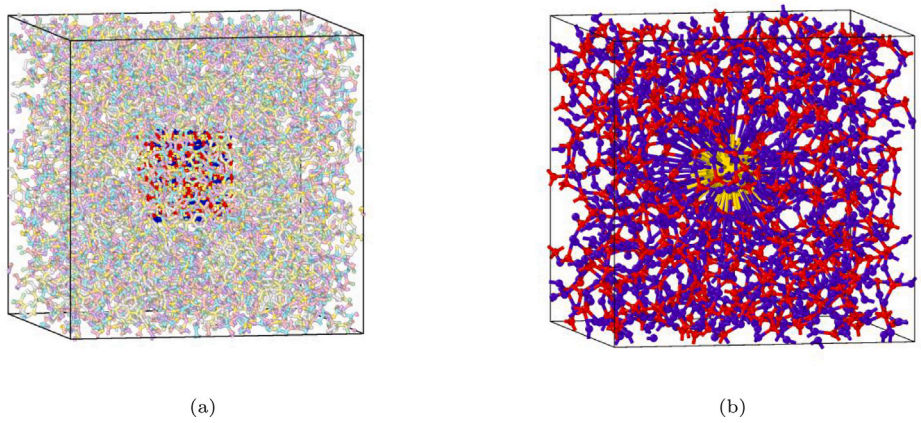

Fig. 13. Simulation boxes of cured boehmite/epoxy nanocomposites, each with dimensions of 60 × 60 × 60 Å^3, for (a) the all-atom model and (b) the CG model.

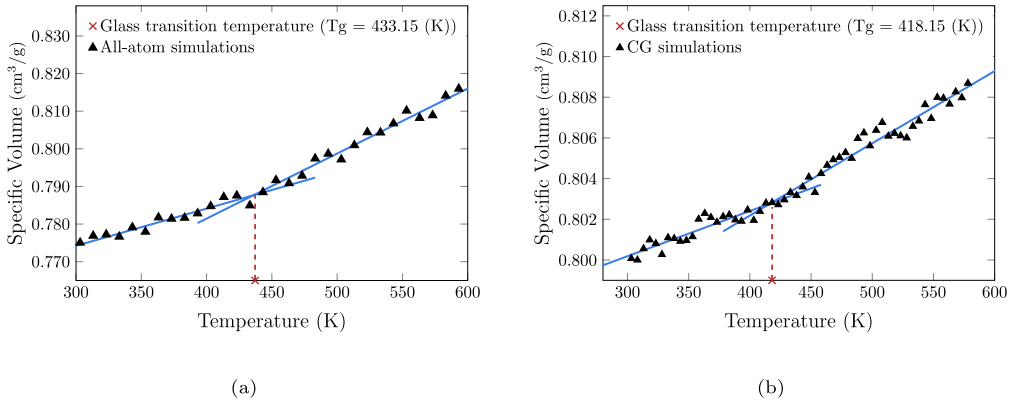

Fig. 14. Specific volume–temperature curves of pure epoxy obtained using (a) the all-atom model and (b) the CG model.

bending interactions, respectively, while LJ potentials are applied for non-bond interactions. The truncation distance for the LJ potential is set at 2.5σ [73]. The steps for construction, curing, equilibration, and the tensile simulation procedure are explained in detail in Section 2.3. Both the all-atom and CG simulations are repeated for three different temperatures and two different strain rates.

To evaluate the predictive capability of the ANN-calibrated CG model, the mass density and the glass transition temperature predicted by the model have been compared with those obtained from all-atom simulations. As shown in Figs. 14(a) and 14(b), the value of Tg for pure epoxy is presented using three configurations for both all-atom and CG models. The mass density predicted by CG simulations agrees

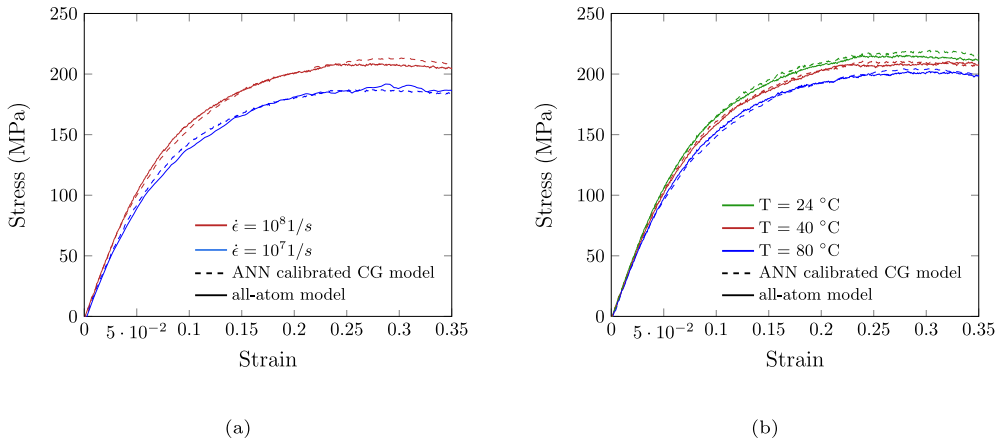

Fig. 15. Average stress–strain curves of pure epoxy obtained using the all-atom and ANN-calibrated CG models at (a) two different strain rates and (b) three different temperatures.

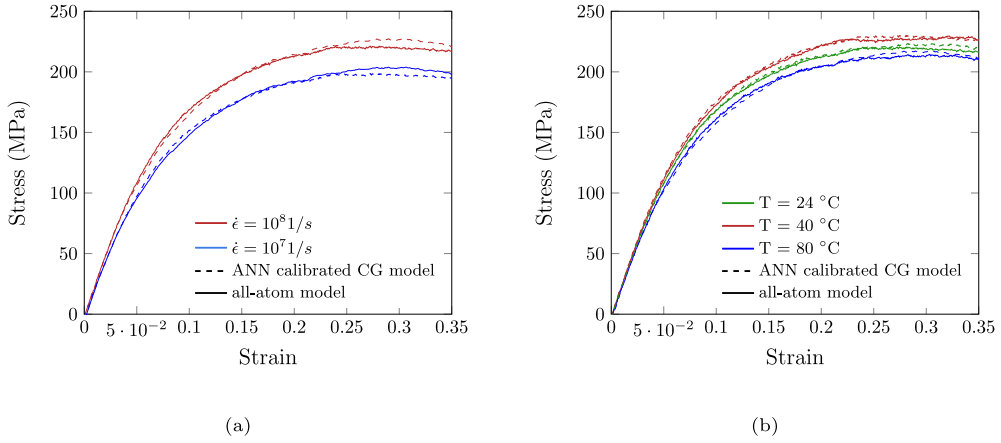

Fig. 16. Average stress–strain curves of BNP (6 wt%)/epoxy nanocomposites obtained using the all-atom and ANN-calibrated CG models at (a) two different strain rates and (b) three different temperatures.

well with that from all-atom simulations across a wide temperature range of 300 to 600 K, recording values of 418.15 K for the CG model and 433.15 K for the all-atom model. These values change to 415 K for the CG model and 431 K for the all-atom model in the case of the BNP/epoxy nanocomposite. The glass transition temperatures obtained from CG and all-atom simulations for both the pure epoxy and the nanocomposite are consistent with the experimental data reported in [4], with a recorded value of 426.15 K for the pure epoxy and approximately 423 K for the BNP/epoxy nanocomposite.

All-atom and CG simulations were performed to display the average stress–strain curves of pure epoxy at two different strain rates, $\dot{\epsilon} = 10^7 1/\text{s}$ and $\dot{\epsilon} = 10^8 1/\text{s}$, at room temperature, as shown in Fig. 15(a). The average stress–strain curves of the pure epoxy at three different temperatures — 24, 40, and 80 °C — at a strain rate of $\dot{\epsilon} = 10^8 1/\text{s}$ are illustrated in Fig. 15(b). As can be seen, the predicted stress–strain response of the pure epoxy using the CG models aligns very well with those obtained from the all-atom models.

In the next step, the average stress–strain relationship of the BNP(6 wt%)/epoxy nanocomposite at different strain rates and temperatures are compared using all-atom and CG simulations. Figs. 16(a) show the stress–strain relationships of the BNP(6 wt%)/epoxy nanocomposite at strain rates of $\dot{\epsilon} = 10^7$ 1/s and $\dot{\epsilon} = 10^8$ 1/s using both models. Additionally, to evaluate the predictive capability of the ANN-calibrated CG model, the predicted stress–strain curves are compared with those from all-atom simulations at temperatures of 24, 40, and 80 °C in Fig. 16(b). As a conclusion, Fig. 16 confirms that the ANN-informed CG model of BNP/epoxy nanocomposite agrees well with the all-atom model. These verification results allow us to use the suggested ANN-calibrated CG model to study the fracture properties of nanoparticle-reinforced epoxy resin nanocomposites.

5.3. Numerical results

The following sections explore how various parameters impact the fracture behavior of the nanocomposites using the proposed CG model. These investigations focus on the RVE size, nanoparticle weight fraction, and agglomerate size. Examining the RVE size and agglomerate size helps ensure that the simulations accurately reflect the overall mechanical properties of the material. Analyzing the nanoparticle weight fraction is critical for optimizing the balance between material strength and flexibility.

5.3.1. Effect of volume element

We first study the effect of volume element (VE) size on the force–displacement curve of BNP/epoxy nanocomposite specimens. In the simulations, single-edge-notched panels with a thickness of B and an initial crack length a, as depicted in Fig. 17(a), are simulated to measure the fracture properties. To generate the CG model, epoxy and hardener are randomly placed in a simulation box with periodic boundary conditions. The system, before curing, is subjected to energy minimization to find the global minimum energy configuration. The curing process and preparation of the equilibrated system are then performed as described in Section 3. After the curing simulation, a single-edge crack, measuring 40% of the length and a width of 6 Å, is created in the middle of the simulation box, as shown in Fig. 17(b). To create this crack configuration, all beads and bonds within

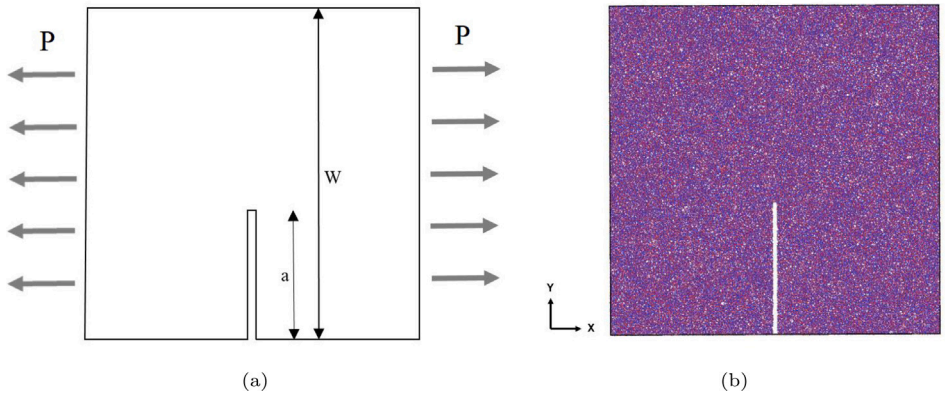

Fig. 17. (a) Schematic of a single-edge notched panel under tensile loading and (b) periodic simulation box of pure epoxy with dimensions 650 × 650 × 160 Å^3.

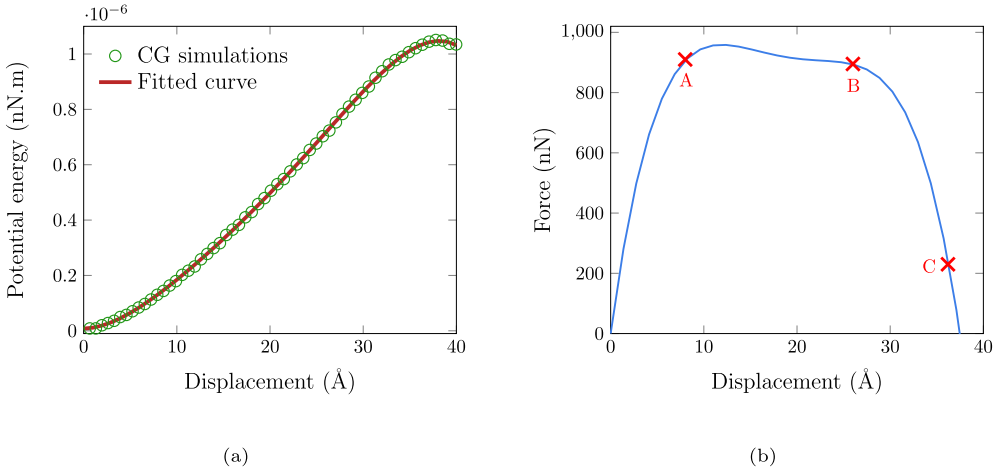

Fig. 18. (a) Variation of potential energy with displacement for pure epoxy with dimensions of 650 × 650 × 160 Å^3, and (b) load–displacement curve for pure epoxy using the CG model. Fracture propagation in the pure epoxy at points indicated by red crosses is illustrated in Fig. 19.

the crack region are deleted, followed by another round of energy minimization. The system is then relaxed using an NPT simulation at room temperature and atmospheric pressure for 2 ns.

In the next step, tensile deformation is applied in a direction that increases the box length at a constant displacement rate, and the coordinates of the CG beads are remapped at every timestep accordingly. Meanwhile, stresses in the lateral directions, perpendicular to the tensile direction, are maintained at zero to accommodate natural Poisson contraction. Bond breakage is also captured using the Morse potential presented in Eq. (2). It is worth noting that the tensile deformation described here is distinct from that applied to simulation boxes without notches, as detailed in Section 2.3.

The fracture simulation is initially performed on pure epoxy specimens. Fig. 17(b) shows a 650 × 650 × 160 Å^3 simulation box containing 215,664 beads, which corresponds to an all-atom system with 3,666,288 atoms. To predict K_I, it is necessary to establish the relationship between force and displacement. For this purpose, a tensile load with a constant displacement rate is applied to the system to observe the variation in potential energy versus displacement. The force–displacement response is then derived from the first derivative of the potential energy with respect to displacement. During the simulation, stresses perpendicular to the tensile direction are maintained at atmospheric pressure using an NPT ensemble. Fig. 18(a) presents the potential energy variation of the system versus displacement, from which the force–displacement curve is obtained, as shown in Fig. 18(b).

The propagation of cracks at different load levels is illustrated in Fig. 19, which shows that the crack growth occurs along the ligament of the initial notch. This observation allows us to conclude that mode I fracture is dominant, and we can extract it from the load–displacement curve. The fracture simulation is conducted at room temperature with a displacement rate set at 325 m/s. After obtaining the force–displacement response, the mode I stress intensity factor for the specimen is calculated using the following equation [72]:

$$K_I = \frac{P}{B\sqrt{W}} \frac{\sqrt{2\tan\frac{\pi a}{2W}}}{\cos\frac{\pi a}{2W}} [0.752 + 2.02(\frac{a}{W}) + 0.37(1 - \sin\frac{\pi a}{2W})^3], \quad (13)$$

where B is the panel thickness, and P, W, and a are defined in Fig. 18(a).

In the simulations, periodic boundary conditions are used to eliminate size effects. Although these conditions help remove artifacts caused by unwanted boundaries, they introduce the artifact of periodic conditions. For amorphous polymer systems, the motion of one molecule affects other molecules placed around it [74]. The long-range interactions between molecules demonstrate an extrusive size effect in simulations. To explore the size dependency of the epoxy system, we increased the side lengths of the simulation box from 300 to 650 Å, while keeping the thickness constant at 160 Å. The simulation results, shown in Fig. 20, demonstrate an increase in the mode I stress intensity factor of the epoxy systems with increasing VE size. Here, the data represent the mean value of 9 simulations at room temperature. Observing only a slight convergence in Fig. 20, we have decided to consider the largest possible volume element that the computational time allows as an representative volume element (RVE) to continue the study, keeping in mind that this RVE is not large enough to definitively report the stress intensity factor.

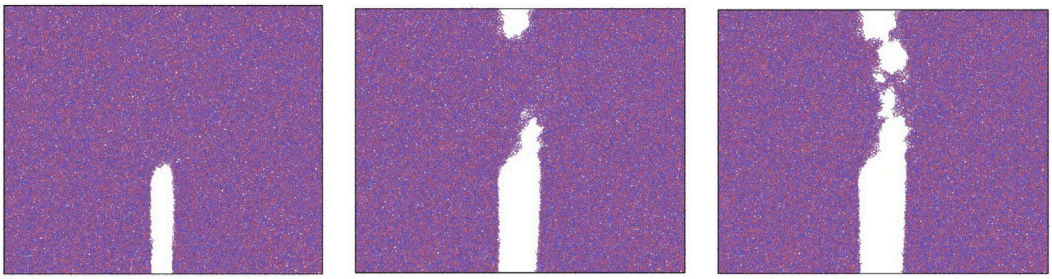

Fig. 19. Fracture propagation in pure epoxy at (a) $\Delta = 8$ Å, (b) $\Delta = 26$ Å, and (c) $\Delta = 36$ Å. Snapshots correspond to the points specified in Fig. 18.

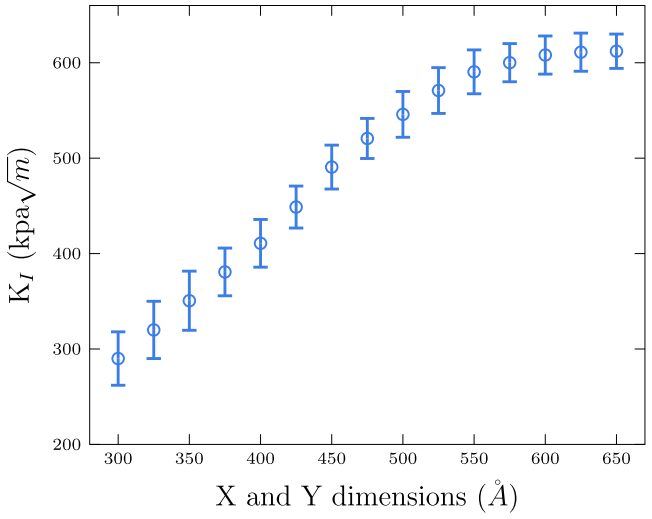

Fig. 20. Variation of K_I of a pure epoxy system with respect to the simulation box side length.

It is noteworthy, that while CG simulations are not suitable for predicting the macro-scale fracture properties of polymer nanocomposites, they remain invaluable for qualitative analyses of key factors such as nanoparticle weight fraction and agglomeration. These aspects are crucial for designing optimized nanocomposites. CG models provide critical insights that inform continuum-level or multiscale models, effectively bridging nanoscale behaviors with macro-scale fracture properties. By enabling computationally efficient predictions of macro-scale behavior based on nanoscale data, they link fundamental mechanisms to practical applications, playing a vital role in the design of high-performance, reliable nanocomposites.

5.3.2. *Effect of agglomerate size*

As mentioned earlier, boehmite nanoparticles typically have a tendency to form agglomerates. To investigate how the size of these agglomerates affects the fracture properties of nanocomposites, we systematically increase the average diameter of the agglomerates. This process continues until a point of convergence is observed, indicating that further increases in size no longer significantly affect the material's fracture behavior. This approach helps to determine the optimal agglomerate size for enhancing the structural integrity and toughness of the nanocomposite.

In the simulations, the box lengths in the x- and y-directions are set to 650 Å, while the thickness is maintained at 160 Å. The initial crack length and width are 260 Å and 6 Å, respectively, and the BNP weight fraction is consistently held at 5wt%. The average diameter of the agglomerates increases from 23 to 100 Å as the number of BNPs increases from 3 to 80, as depicted in Fig. 21. The simulation details and conditions replicate those of previous simulations. The effects of agglomeration size on the mode I stress intensity factor are illustrated in Fig. 22. The simulation results indicate that the average magnitude of K_I converges to approximately 693 kPa$\sqrt{\text{m}}$, as the agglomerate size increases to 100 Å. In subsequent simulations, agglomerates containing 80 BNPs with an average diameter of 100 Å are considered sufficiently large to serve as representative.

5.3.3. *Effect of nanoparticle weight fraction*

We next explore the impact of nanoparticle weight fraction on the force–displacement response of BNP/epoxy nanocomposites. The RVE size, initial crack length, and mass density are consistent with those detailed in earlier subsections. In this study, the BNP weight fraction varies from 0 to 15 wt%. Figs. 23(a) and 23(b) provide top views and perspectives of a CG model for a BNP/epoxy nanocomposite with a 10% BNP weight fraction, serving as a representative example for this analysis.

Fig. 24 presents the load–displacement behavior of pure epoxy resin and its BNP-reinforced nanocomposites under tensile loading, as predicted by the CG model. The results reveal that adding BNPs to the epoxy matrix increases the material's resistance to fracture in the presence of cracks. Fig. 24 confirms that the BNP/epoxy nanocomposite becomes more resistant to fracture as the nanoparticle weight fraction increases from 0 to 15 wt%. Additionally, it is shown that the area under the load–displacement curve, and thus the maximum force, is higher for the dispersed BNP (15 wt%) compared to the agglomerated BNP (15 wt%). Therefore, as expected, the epoxy matrix demonstrates greater fracture resistance when the BNPs do not form agglomerates.

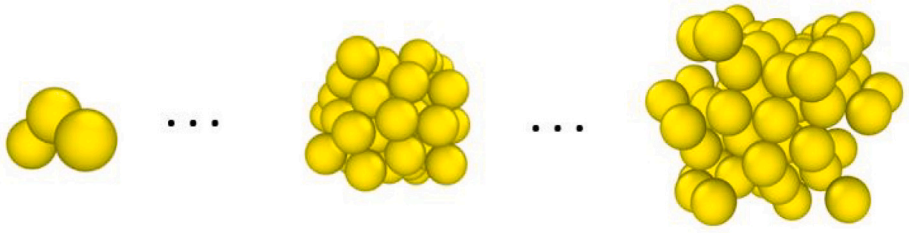

Fig. 21. Illustration of a single agglomerate containing (a) 3, (b) 40, and (c) 80 BNPs.

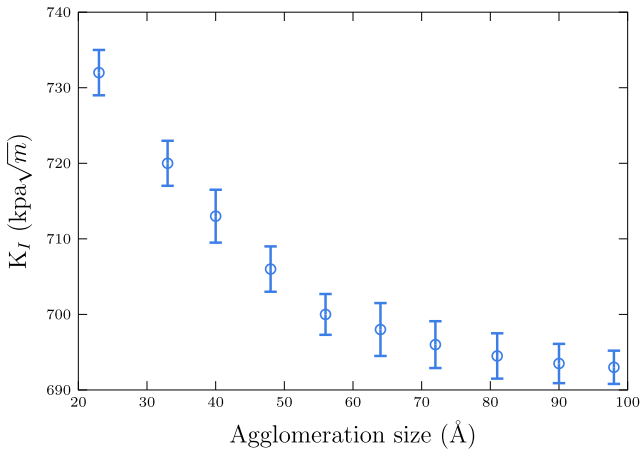

Fig. 22. Variation of K_I with increasing x- and y-dimensions of BNP (5 wt%)/epoxy nanocomposites, while maintaining a constant simulation box width set to 650 Å.

In experiments, some BNPs are uniformly distributed, while other nanoparticles form agglomerates, as noted in [4]. This results in a non-uniform dispersion of BNPs within the epoxy matrix. However, due to the limited length scale and the use of periodic boundary conditions, our CG simulations can only model either fully distributed or fully agglomerated particles. Although this simplification leads to deviations between the numerical predictions and experimental data, the CG model still allows us to qualitatively predict lower and upper bounds for the fracture properties of BNP/epoxy nanocomposites. Fig. 26 includes snapshots of the pure epoxy matrix and BNP (15 wt%)/epoxy nanocomposites with fully agglomerated and well-dispersed nanoparticles at a displacement of 36 Å. It is evident that BNP/epoxy nanocomposites exhibit enhanced strength in the presence of cracks compared to pure epoxy.

Fig. 25 illustrates the effect of nanoparticle distribution on the stress intensity factor across different BNP weight fractions. The average K_I for BNP/epoxy nanocomposites increases from 600 to 693 kPa$\sqrt{\text{m}}$ for agglomerated BNPs, and to 732 kPa$\sqrt{\text{m}}$ for fully dispersed BNPs, as the BNP weight fraction increases from 0 to 5 wt%. This corresponds to percentage increases of 15% and 22% compared to pure epoxy, respectively. As the weight fraction of BNPs increases to 10 wt%, the mode I stress intensity factor rises further to 738 and 786 kPa$\sqrt{\text{m}}$ for agglomerated and fully dispersed BNPs, showing deviations of 23% and 31% compared to pure epoxy, respectively. The calculated average values of K_I for the BNP (15 wt%)/epoxy nanocomposite are 804 and 853 kPa$\sqrt{\text{m}}$ for agglomerated and fully dispersed BNPs, respectively, showing percentage increases of about 34% and 42% compared to pure epoxy. Notably, the observed behavior suggests that the dispersion and agglomeration of BNPs are concentration-dependent. At 5 and 10 wt%, fewer BNPs result in intermediate behavior due to weaker interparticle interactions and lower matrix saturation. At 15 wt%, the higher concentration promotes the formation of smaller, more dispersed agglomerates, which align the system behavior closer to that of fully dispersed BNPs.

6. Conclusions

This research introduces an ANN-based optimization framework for calibrating CG models tailored to nanoparticle-reinforced polymers. The approach defines an objective function as the total squared error between thermo-mechanical properties predicted by the ANN-trained CG model and those obtained from all-atom simulations. This method significantly reduces computational cost while maintaining high fidelity in predicting the thermo-mechanical properties of polymer nanocomposites across a wide temperature range. This study integrates ANN-based optimization with CG simulations to tackle challenges in force field parameterization, improving predictive accuracy and ensuring temperature transferability. This intermediate approach balances accuracy and cost, improving upon traditional CG methods through machine learning optimization while avoiding the data and computational demands of machine learning force fields (MLFFs), making it ideal for qualitative studies of nanocomposite fracture behavior. The ANN model is tailored to the DGEBA/MTHPA epoxy system with BNPs. While the methodology is generalizable, predicting fracture properties for a different polymer matrix would require retraining the model with new all-atom simulation data. Nevertheless, qualitative insights, such as the role of nanoparticle dispersion in enhancing fracture resistance, may apply broadly to polymer nanocomposites.

Leveraging the optimized CG model, we investigated the effects of BNP weight fraction and distribution (agglomerated vs. dispersed) on the fracture properties of epoxy nanocomposites. Simulations of two extreme cases — fully dispersed and agglomerated BNPs — provided bounds for the stress intensity factor. Experimental K_I values for nanocomposites with non-uniform BNP dispersion fell within these bounds, validating the model's capability to capture the influence of agglomeration on fracture properties. For instance, a 15 wt% BNP content increased K_I by 39% experimentally, aligning with simulation results showing increases of 42% for dispersed and 34% for agglomerated nanoparticles. Both numerical simulation and experimental results indicate that nanoparticle additives significantly improve the fracture properties of the epoxy matrix. This numerical–experimental comparison confirms that the proposed machine-learning-assisted CG model effectively captures the impact of nanoparticle agglomeration on the fracture properties of polymer nanocomposites.

While CG models may not deliver exact quantitative predictions for macro-scale fracture properties, they are invaluable for obtaining

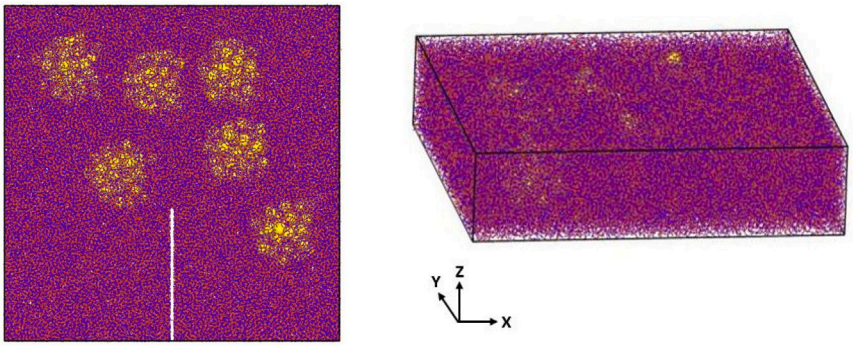

Fig. 23. Simulation box of BNP (10 wt%)/epoxy nanocomposites with dimensions of 650 × 650 × 160Å^3 featuring an initial crack: (a) top view and (b) perspective view.

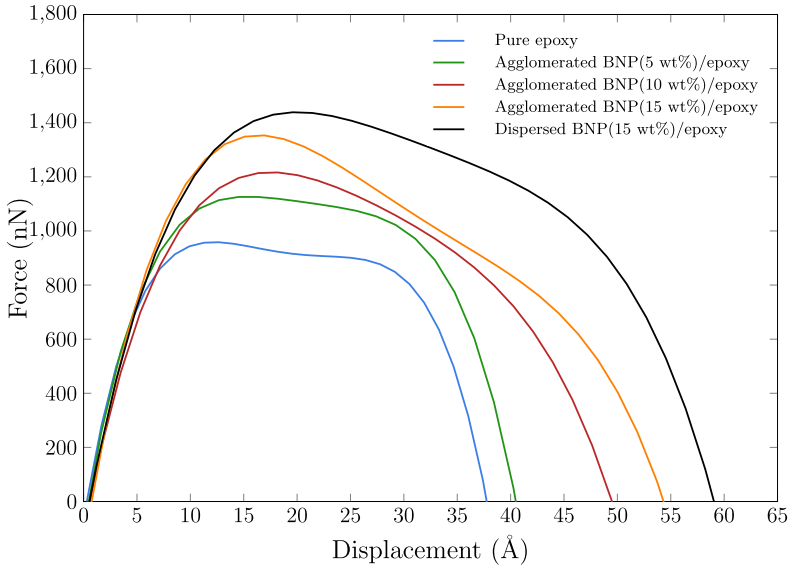

Fig. 24. Force–displacement response of agglomerated BNP/epoxy nanocomposites at varying nanoparticle weight fractions.

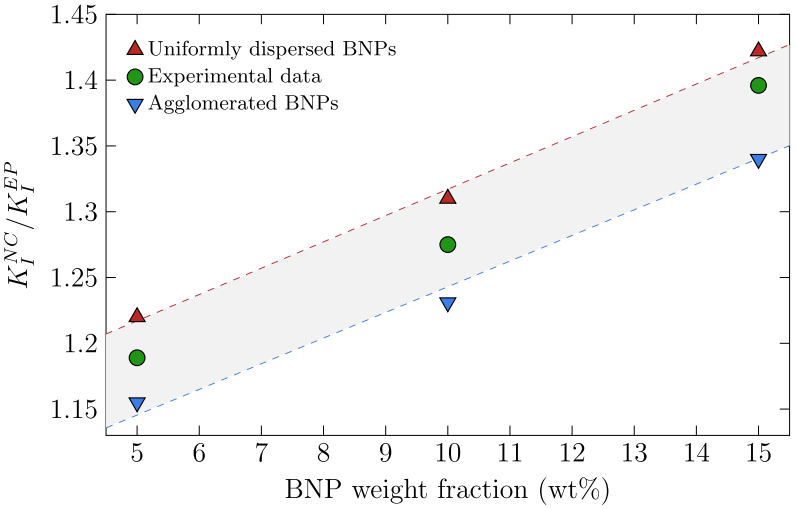

Fig. 25. Effect of nanoparticle distribution on the stress intensity factor across different BNP weight fractions.

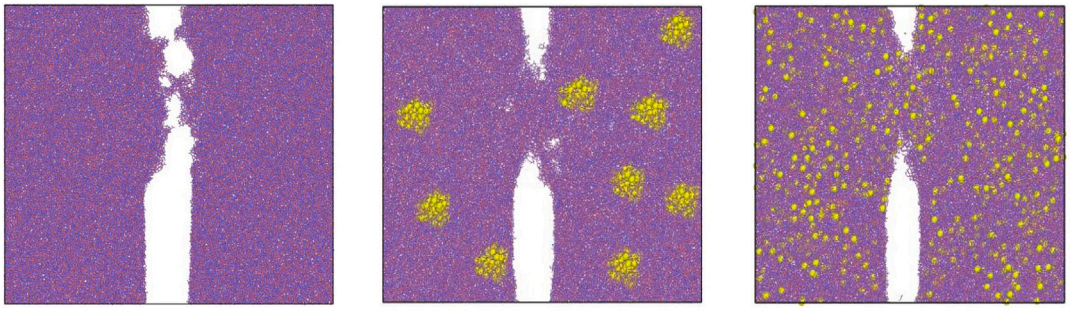

Fig. 26. Snapshots of (a) pure epoxy, (b) agglomerated BNP (15 wt%)/epoxy nanocomposite, and (c) randomly distributed BNP (15 wt%)/epoxy nanocomposite at a displacement of 36 Å.

qualitative insights into the mechanisms governing polymer nanocomposites' behavior. The MLP's R^2 of 0.8 reflects a well-balanced compromise in predicting various properties. Meanwhile, future research could investigate property-specific ANNs to improve individual accuracies, although this may come at a higher computational cost. Future work could explore neural networks as direct CG force fields,

predicting forces and energies from configurations, to potentially improve multi-property accuracy, though this would require increased data and computational investment compared to our current approach. Additionally, future work could also explore hybrid models integrating constitutive equations with machine learning, combining physical grounding with data-driven flexibility to further improve predictions of fracture properties in polymer nanocomposites.

CRediT authorship contribution statement

Atiyeh Hente: Writing – original draft, Visualization, Validation, Software, Methodology, Investigation, Formal analysis, Data curation, Conceptualization. **Behrouz Arash:** Writing – review & editing, Supervision, Investigation, Data curation, Conceptualization. **Maximilian Jux:** Writing – review & editing, Investigation, Data curation. **Raimund Rolfes:** Writing – review & editing, Supervision, Resources, Funding acquisition.

Declaration of generative AI/AI-assisted technologies in the writing process

During the preparation of this work, the authors used ChatGPT to enhance English proficiency and improve grammar. After using this tool/service, the authors reviewed and edited the content as needed and take full responsibility for the content of the publication.

Declaration of competing interest

The authors declare that they have no known competing financial interests or personal relationships that could have appeared to influence the work reported in this paper.

Acknowledgments

The present work originates from the Research Unit FOR 2021: ‘‘Acting Principles of Nano-Scaled Matrix Additives for Composite Structures’’, funded by the German Research Foundation (DFG). The authors express their gratitude for this financial support. Additionally, the authors acknowledge the support of the LUIS scientific computing cluster, funded by Leibniz University Hannover and the Lower Saxony Ministry of Science and Culture (MWK), Germany.

Data availability

Data will be made available on request.

References

[1] S.H. Zaferani, Introduction of polymer-based nanocomposites, in: Polymer-Based Nanocomposites for Energy and Environmental Applications, Elsevier, 2018, pp. 1–25.
[2] B. Arash, Q. Wang, V.K. Varadan, Finite element analysis of polymer nanocomposites: Effects of nanoparticle dispersion and alignment on mechanical properties, Compos. Part B: Eng. 202 (2021) 108–117.
[3] M. Jux, B. Finke, T. Mahrholz, M. Sinapius, A. Kwade, C. Schilde, Effects of Al(OH)O nanoparticle agglomerate size in epoxy resin on tension, bending, and fracture properties, J. Nanoparticle Res. 19 (4) (2017) 139.
[4] M.G.Z. Khorasani, D. Silbernagl, P. Szymoniak, V.-D. Hodoroaba, H. Sturm, The effect of boehmite nanoparticles (γ-AlOOH) on nanomechanical and thermomechanical properties correlated to crosslinking density of epoxy, Polymer 164 (2019) 174–182.
[5] M. Jux, J. Fankhänel, B. Daum, T. Mahrholz, M. Sinapius, R. Rolfes, Mechanical properties of epoxy/boehmite nanocomposites in dependency of mass fraction and surface modification-An experimental and numerical approach, Polymer 141 (2018) 34–45.
[6] C. Arlt, W. Exner, U. Riedel, H. Sturm, J.M. Sinapius, Nanoscaled boehmites’ modes of action in a polymer and its carbon fiber reinforced plastic, in: Acting Principles of Nano-Scaled Matrix Additives for Composite Structures, Springer, 2021, pp. 367–376, http://dx.doi.org/10.1007/978-3-030-68523-2_16.
[7] Z. Wu, Q. Zhuo, T. Sun, Z. Wang, Mechanical properties of epoxy resins reinforced with synthetic boehmite (AlOOH) nanosheets, J. Appl. Polym. Sci. 132 (5) (2015).
[8] J. Fankhänel, B. Arash, R. Rolfes, Elastic interphase properties of nanoparticle/epoxy nanocomposites: A molecular dynamics study, Compos. Part B: Eng. 176 (2019) 107211.
[9] M. Sangermano, F. Deorsola, D. Fabiani, G. Montanari, G. Rizza, Epoxy-boehmite nanocomposites as new insulating materials, J. Appl. Polym. Sci. 114 (4) (2009) 2541–2546.
[10] M. Dong, Y. Sun, D.J. Dunstan, R.J. Young, D.G. Papageorgiou, Mechanical reinforcement from two-dimensional nanofillers: Model, bulk and hybrid polymer nanocomposites, Nanoscale (2024).
[11] N. Wiedyaningsih, Enhancing fracture toughness in polymeric materials through the integration of nanocomposites, IJMS 5 (1) (2024) 22–24.
[12] R. Unger, W. Exner, B. Arash, R. Rolfes, Non-linear viscoelasticity of epoxy resins: Molecular simulation-based prediction and experimental validation, Polymer 180 (2019) 121722.
[13] R. Unger, B. Arash, W. Exner, R. Rolfes, Effect of temperature on the viscoelastic damage behaviour of nanoparticle/epoxy nanocomposites: Constitutive modelling and experimental validation, Polymer 191 (2020) 122265.
[14] T. Katafiasz, E. Greenhalgh, G. Allegri, S. Pinho, P. Robinson, The influence of temperature and moisture on the mode I fracture toughness and associated fracture morphology of a highly toughened aerospace CFRP, Compos. Part A: Appl. Sci. Manuf. 142 (2021) 106241.
[15] S. Chopra, K.A. Deshmukh, A.D. Deshmukh, C. Gogte, D. Peshwe, Prediction, evaluation and mechanism governing interphase strength in tensile fractured PA-6/MWCNT nanocomposites, Compos. Part A: Appl. Sci. Manuf. 112 (2018) 255–262.
[16] Y. Li, S. Wang, Q. Wang, M. Xing, Enhancement of fracture properties of polymer composites reinforced by carbon nanotubes: A molecular dynamics study, Carbon 129 (2018) 504–509.
[17] M.Y. Zhou, J. Liu, L.Q. Zhang, Structure and properties of polymer/two-dimensional nanomaterials studied via molecular dynamics simulation: A review, Mol. Syst. Des. Eng. 8 (1) (2023) 11–31.
[18] G. Hou, R. Ren, W. Shang, Y. Weng, J. Liu, Molecular dynamics simulation of polymer nanocomposites with supramolecular network constructed via functionalized polymer end-grafted nanoparticles, Polymers 15 (15) (2023) 3259.
[19] K. Hagita, H. Morita, H. Takano, Molecular dynamics simulation study of a fracture of filler-filled polymer nanocomposites, Polymer 99 (2016) 368–375.
[20] S. Roy, T. Sohail, Fracture simulation in polymer nanocomposites using molecular dynamics, in: Proceedings of the American Society for Composites—Thirty-Sixth Technical Conference on Composite Materials, 2021, pp. 1–5.
[21] B. Arash, S. Zakavati Gharagozlou, B. Bahtiri, M. Jux, R. Rolfes, Phase-field modeling of fracture in viscoelastic–viscoplastic thermoset nanocomposites under cyclic and monolithic loading, Eng. Comput. (2024).
[22] V. Agrawal, G. Arya, J. Oswald, Simultaneous iterative boltzmann inversion for coarse-graining of polyurea, Macromolecules 47 (10) (2014) 3378–3389.
[23] P. Huang, L. Shen, Y. Gan, F. Maggi, A. El-Zein, Numerical investigation of microscale dynamic contact angles of the CO2–water–silica system using coarse-grained molecular approach, Comput. Mech. 66 (3) (2020) 707–722.
[24] H. Wang, K. Jin, C. Wang, X. Guo, Z. Chen, J. Tao, Effect of fiber surface functionalization on shear behavior at carbon fiber/epoxy interface through molecular dynamics analysis, Compos. Part A: Appl. Sci. Manuf. 126 (2019) 105611.
[25] B. Arash, H.S. Park, T. Rabczuk, Coarse-grained model of the J-integral of carbon nanotube reinforced polymer composites, Carbon 96 (2016) 1084–1092.
[26] J. Cui, F. Zeng, D. Wei, Y. Wang, Unraveling the effects of geometrical parameters on dynamic impact responses of graphene reinforced polymer nanocomposites using coarse-grained molecular dynamics simulations, Phys. Chem. Chem. Phys. 26 (28) (2024) 19266–19281.
[27] F. Hu, Y. Nie, F. Li, J. Liu, Y. Gao, W. Wang, L. Zhang, Molecular dynamics simulation study of the fracture properties of polymer nanocomposites filled with grafted nanoparticles, Phys. Chem. Chem. Phys. 21 (21) (2019) 11320–11328.
[28] J. Liu, J. Shen, Y. Gao, H. Zhou, Y. Wu, L. Zhang, Detailed simulation of the role of functionalized polymer chains on the structural, dynamic and mechanical properties of polymer nanocomposites, Soft Matter 10 (44) (2014) 8971–8984.
[29] A. Arora, T.-S. Lin, B.D. Olsen, Coarse-grained simulations for fracture of polymer networks: Stress versus topological inhomogeneities, Macromolecules 55 (1) (2021) 4–14.
[30] Y. Higuchi, K. Saito, T. Sakai, J.P. Gong, M. Kubo, Fracture process of double-network gels by coarse-grained molecular dynamics simulation, Macromolecules 51 (8) (2018) 3075–3087.
[31] N. Hu, Y. Wang, R. Ma, W. Zhang, B. Li, X. Zhao, L. Zhang, Y. Gao, Optimizing the fracture toughness of a dual cross-linked hydrogel via molecular dynamics simulation, Phys. Chem. Chem. Phys. 24 (29) (2022) 17605–17614.
[32] S.J. Marrink, H.J. Risselada, S. Yefimov, D.P. Tieleman, A.H. De Vries, The MARTINI force field: Coarse grained model for biomolecular simulations, J. Phys. Chem. B 111 (27) (2007) 7812–7824.
[33] D. Reith, M. Pütz, F. Müller-Plathe, Deriving effective mesoscale potentials from atomistic simulations, J. Comput. Chem. 24 (13) (2003) 1624–1636.

[34] A. Aramoon, T.D. Breitzman, C. Woodward, J.A. El-Awady, Coarse-grained molecular dynamics study of the curing and properties of highly cross-linked epoxy polymers, J. Phys. Chem. B 120 (35) (2016) 9495–9505.
[35] B. Arash, H.S. Park, T. Rabczuk, Mechanical properties of carbon nanotube reinforced polymer nanocomposites: A coarse-grained model, Compos. Part B: Eng. 80 (2015) 92–100.
[36] A.A. Mousavi, B. Arash, X. Zhuang, T. Rabczuk, A coarse-grained model for the elastic properties of cross linked short carbon nanotube/polymer composites, Compos. Part B: Eng. 95 (2016) 404–411.
[37] A. Prasad, T. Grover, S. Basu, Coarse–grained molecular dynamics simulation of cross–linking of DGEBA epoxy resin and estimation of the adhesive strength, Int. J. Eng. Sci. Technol. 2 (4) (2010) 17–30.
[38] T. Aoyagi, Optimization of the elastic properties of block copolymers using coarse-grained simulation and an artificial neural network, Comput. Mater. Sci. 207 (2022) 111286.
[39] B. Bahtiri, B. Arash, S. Scheffler, M. Jux, R. Rolfes, A machine learning-based viscoelastic–viscoplastic model for epoxy nanocomposites with moisture content, Comput. Methods Appl. Mech. Engrg. 415 (2023) 116293.
[40] B. Bahtiri, B. Arash, S. Scheffler, M. Jux, R. Rolfes, A thermodynamically consistent physics-informed deep learning material model for short fiber/polymer nanocomposites, Comput. Methods Appl. Mech. Engrg. 427 (2024) 117038.
[41] A.A. Mousavi, B. Arash, R. Rolfes, Optimization assisted coarse-grained modeling of agglomerated nanoparticle reinforced thermosetting polymers, Polymer 225 (2021) 123741.
[42] K.K. Bejagam, S. Singh, Y. An, S.A. Deshmukh, Machine-learned coarse-grained models, J. Phys. Chem. Lett. 9 (16) (2018) 4667–4672.
[43] K. Duan, Y. He, Y. Li, J. Liu, J. Zhang, Y. Hu, R. Lin, X. Wang, W. Deng, L. Li, Machine-learning assisted coarse-grained model for epoxies over wide ranges of temperatures and cross-linking degrees, Mater. Des. 183 (2019) 108130.
[44] J. Ruza, W. Wang, D. Schwalbe-Koda, S. Axelrod, W.H. Harris, R. Gómez-Bombarelli, Temperature-transferable coarse-graining of ionic liquids with dual graph convolutional neural networks, J. Chem. Phys. 153 (16) (2020) 164501.
[45] T. Lemke, C. Peter, Neural network based prediction of conformational free energies-a new route toward coarse-grained simulation models, J. Chem. Theory Comput. 13 (12) (2017) 6213–6221.
[46] J. Wang, S. Olsson, C. Wehmeyer, A. Pérez, N.E. Charron, G. De Fabritiis, F. Noé, C. Clementi, Machine learning of coarse-grained molecular dynamics force fields, ACS Central Sci. 5 (5) (2019) 755–767.
[47] T.D. Loeffler, T.K. Patra, H. Chan, S.K. Sankaranarayanan, Active learning a coarse-grained neural network model for bulk water from sparse training data, Mol. Syst. Des. Eng. 5 (5) (2020) 902–910.
[48] T.D. Loose, P.G. Sahrmann, T.S. Qu, G.A. Voth, Coarse-graining with equivariant neural networks: A path toward accurate and data-efficient models, J. Phys. Chem. B 127 (49) (2023) 10564–10572.
[49] A.D.S. Costa, I. Mitnikov, M. Geiger, M. Ponnapati, T. Smidt, J. Jacobson, Ophiuchus: Scalable modeling of protein structures through hierarchical coarse-graining SO (3)-equivariant autoencoders, 2023, arXiv preprint arXiv:2310.02508.
[50] Y. Yu, J. Harlim, D. Huang, Y. Li, Learning coarse-grained dynamics on graph, 2024, arXiv preprint arXiv:2405.09324.
[51] E. Ricci, N. Vergadou, Integrating machine learning in the coarse-grained molecular simulation of polymers, J. Phys. Chem. B 127 (11) (2023) 2302–2322.
[52] A. Mousavi, J. Fankhänel, B. Arash, R. Rolfes, A multi-scale framework for the prediction of the elastic properties of nanocomposites, in: Acting Principles of Nano-Scaled Matrix Additives for Composite Structures, Springer, 2021, pp. 179–207.
[53] L. Martínez, R. Andrade, E. Birgin, J. Martínez, Software news and update PACKMOL: A package for building initial configurations for molecular dynamics simulations, J. Comput. Chem. 30 (13) (2009) 2157–2164.
[54] S.L. Mayo, B.D. Olafson, W.A. Goddard, A generic force field for molecular simulations, J. Phys. Chem. 94 (26) (1990) 8897–8909.
[55] J. Lebowitz, D. Zomick, Mixtures of hard spheres with nonadditive diameters: Some exact results and solution of PY equation, J. Chem. Phys. 54 (8) (1971) 3335–3346.
[56] S. Melchionna, G. Ciccotti, B. Lee Holian, Hoover NPT dynamics for systems varying in shape and size, Mol. Phys. 78 (3) (1993) 533–544.
[57] T. Schneider, E. Stoll, Molecular-dynamics study of a three-dimensional one-component model for distortive phase transitions, Phys. Rev. B 17 (3) (1978) 1302.
[58] A. Stukowski, Visualization and analysis of atomistic simulation data with OVITO–the open visualization tool, Modelling Simul. Mater. Sci. Eng. 18 (1) (2009) 015012.
[59] S. Plimpton, Fast parallel algorithms for short-range molecular dynamics, J. Comput. Phys. 117 (1) (1995) 1–19.
[60] R.K. Giri, N. Swaminathan, Role of mapping schemes on dynamical and mechanical properties of coarse-grained models of cis-1, 4-polyisoprene, Comput. Mater. Sci. 208 (2022) 111309.
[61] D. Tunega, H. Pašalić, M. Gerzabek, H. Lischka, Theoretical study of structural, mechanical and spectroscopic properties of boehmite (γ-AlOOH), J. Phys.: Condens. Matter. 23 (40) (2011) 404201.
[62] X. Bokhimi, J. Toledo-Antonio, M. Guzman-Castillo, F. Hernandez-Beltran, Relationship between crystallite size and bond lengths in boehmite, J. Solid State Chem. 159 (1) (2001) 32–40.
[63] A. Kiss, G. Keresztury, L. Farkas, Raman and ir spectra and structure of boehmite (γ-AlOOH). evidence for the recently discarded D172h space group, Spectrochim. Acta Part A: Mol. Spectrosc. 36 (7) (1980) 653–658.
[64] P.M. Atkinson, A.R.L. Tatnall, Introduction neural networks in remote sensing, Int. J. Remote Sens. 18 (4) (1997) 699–709.
[65] T.E. Davis III, P.F. Kurtz, A.W. Gardner, N.B. Carman, Cognitive-behavioral treatment for specific phobias with a child demonstrating severe problem behavior and developmental delays, Res. Dev. Disabil. 28 (6) (2007) 546–558.
[66] M.T. Hagan, M.B. Menhaj, Training feedforward networks with the Marquardt algorithm, IEEE Trans. Neural Netw. 5 (6) (1994) 989–993.
[67] L. Kocis, W.J. Whiten, Computational investigations of low-discrepancy sequences, ACM Trans. Math. Softw. 23 (2) (1997) 266–294.
[68] L. Zhang, J. Han, H. Wang, R. Car, W. E, DeePCG: Constructing coarse-grained models via deep neural networks, J. Chem. Phys. 149 (3) (2018) 034101.
[69] P. Ge, L. Zhang, H. Lei, Machine learning assisted coarse-grained molecular dynamics modeling of meso-scale interfacial fluids, J. Chem. Phys. 158 (6) (2023).
[70] C. Tan, J. Jung, C. Kobayashi, D.U.L. Torre, S. Takada, Y. Sugita, Implementation of residue-level coarse-grained models in GENESIS for large-scale molecular dynamics simulations, PLoS Comput. Biol. 18 (4) (2022) e1009578.
[71] D. Furman, B. Carmeli, Y. Zeiri, R. Kosloff, Enhanced particle swarm optimization algorithm: Efficient training of reaxff reactive force fields, J. Chem. Theory Comput. 14 (6) (2018) 3100–3112.
[72] T.L. Anderson, Fracture Mechanics: Fundamentals and Applications, CRC Press, 2017.
[73] D. Frenkel, B. Smit, Understanding Molecular Simulation: From Algorithms to Applications, Elsevier, 2023.
[74] X. Yang, H. Zhang, L. Li, X. Ji, Corrections of the periodic boundary conditions with rectangular simulation boxes on the diffusion coefficient, general aspects, Mol. Simul. 43 (17) (2017) 1423–1429.